nature communications

Article

https://doi.org/10.1038/s41467-025-56955-y

BBOX1 restrains TBK1-mTORC1 oncogenic signaling in clear cell renal cell carcinoma

Received: 26 February 2024

Accepted: 27 January 2025

Published online: 11 February 2025

Check for updates

Chengheng Liao[1,12] ✉, Lianxin Hu[1,2,12], Liwei Jia[1], Jin Zhou[1], Tao Wang[1], Kangsan Kim[1], Hua Zhong[1,3], Hongwei Yao[1], Lei Dong[4], Lei Guo[4], Qian Liang[1], Cheng Zhang[1], Fangzhou Zhao[1], Jun Fang[1], Hongyi Liu[1], Shina Li[1], Lin Xu[4], Jeremy M. Simon[5,6], Srinivas Malladi[1], Payal Kapur[1,7], James Brugarolas[7,8], Ralph J. DeBerardinis[9,10] & Qing Zhang[1,11] ✉

Clear cell renal cell carcinoma (ccRCC), a metabolic disease originating from renal proximal convoluted tubule (PCT) epithelial cells, remains incompletely understood in terms of its initiating signaling events. Here, we identify γ-butyrobetaine hydroxylase 1 (BBOX1), a key enzyme in carnitine synthesis predominantly expressed in PCT cells, as a tumor suppressor in ccRCC. BBOX1 expression is lost during ccRCC malignant transformation, and its restoration reduces cell viability in physiological medium and inhibits xenograft tumor growth. Transcriptomic analyses reveal that BBOX1 suppresses critical metabolic pathways including mTORC1 signaling and glycolysis in ccRCC. Further, we identify TANK-binding kinase 1 (TBK1) as an essential mediator of mTORC1 and glycolysis activation and as a target of BBOX1-mediated tumor suppression. Mechanistically, BBOX1 disrupts TBK1 activation by preventing its interaction with the upstream activator doublecortin-like kinase 2 (DCLK2). This BBOX1-DCLK2-TBK1 axis unveils an important mechanism in ccRCC metabolic dysregulation and highlights potential therapeutic strategies.

In 2022 there were approximately 79,000 new cases and 13,390 deaths from renal cancer in the United States[1]. The incidence of renal cancer has exhibited a consistent increase over the past several decades, yet the underlying reasons remain unclear[2]. Clear cell renal cell carcinoma (ccRCC), which accounts for 85% of renal cancers, is a lethal disease and classically resistant to chemotherapy[3]. In the majority of ccRCC, von Hippel–Lindau (*VHL*) gene inactivation leads to HIF2α stabilization which is both sufficient and necessary for ccRCC tumor growth[4]. Recent reports showed that specific HIF2α inhibitors, such as PT2399, inhibit primary tumor growth and invasion of a subset of ccRCC[5,6]. However, a significant proportion of ccRCC remains resistant to HIF2α inhibitor treatment[5–8], highlighting the importance of identifying additional therapeutic vulnerabilities.

ccRCC is a metabolic disease with distinctive metabolic features[9,10]. Altered metabolism offers unique opportunities for therapeutic intervention[11]. Specifically, ccRCC is characterized by

[1]Department of Pathology, University of Texas Southwestern Medical Center, Dallas, TX, USA. [2]Department of Urology, Institute of Urologic Science and Technology, The First Affiliated Hospital, School of Medicine, Zhejiang University, Hangzhou, Zhejiang, China. [3]Lyda Hill Department of Bioinformatics, University of Texas Southwestern Medical Center, Dallas, TX, USA. [4]Quantitative Biomedical Research Center, Peter O'Donnell Jr. School of Public Health, University of Texas Southwestern Medical Center, Dallas, TX, USA. [5]Department of Data Science, Dana-Farber Cancer Institute, Boston, MA, USA. [6]Department of Biostatistics, Harvard T.H. Chan School of Public Health, Boston, MA, USA. [7]Kidney Cancer Program, Simmons Comprehensive Cancer Center, University of Texas Southwestern Medical Center, Dallas, TX, USA. [8]Department of Internal Medicine, University of Texas Southwestern Medical Center, Dallas, TX, USA. [9]Children's Medical Center Research Institute, University of Texas Southwestern Medical Center, Dallas, TX, USA. [10]Howard Hughes Medical Institute, University of Texas Southwestern Medical Center, Dallas, TX, USA. [11]Simmons Comprehensive Cancer Center, University of Texas Southwestern Medical Center, Dallas, TX, USA. [12]These authors contributed equally: Chengheng Liao, Lianxin Hu. ✉e-mail: Chengheng.Liao@UTSouthwestern.edu; Qing.Zhang@UTSouthwestern.edu

enhanced aerobic glycolysis and repressed mitochondrial respiration[12–16], indicating glucose metabolism is important for ccRCC development. This glycolytic metabolic reprogramming is driven largely by HIF and the mammalian target of rapamycin complex 1 (mTORC1), which are commonly hyperactivated in ccRCC[17–21]. Notably, VHL inactivation suppresses mitochondria respiration in vivo in a HIF-dependent manner[22]. In addition, while HIF accumulation leads to enhanced lactate production, mTORC1 influences glycolysis by directly phosphorylating key glycolytic enzymes, or indirectly by controlling HIF and MYC, which regulate glycolytic gene expression[17–19]. Understanding the precise regulation of these critical metabolic pathways may identify vulnerabilities providing new opportunities for therapeutic intervention.

γ-Butyrobetaine hydroxylase 1 (BBOX1), a 2-oxoglutarate dependent dioxygenase, hydroxylates γ-butyrobetaine promoting the biosynthesis of carnitine[23]. Carnitine is involved in the transport of fatty acids into mitochondria, where they undergo β-oxidation to provide energy. Thus, BBOX1 regulates lipid metabolism based on its enzymatic activity in carnitine biosynthesis[24]. In addition, large-scale microarray and clinical data analyses have recently implicated BBOX1 in tumorigenesis[25,26]. However, how BBOX1 may be implicated in cancer is unclear. By performing functional phenotypic screening using an unbiased library, we previously revealed that BBOX1 is a potential oncogenic driver overexpressed in triple negative breast cancer (TNBC)[27]. BBOX1 promotes TNBC cell proliferation and tumorigenesis in a non-canonical fashion by controlling the stability of inositol-1,4,5-trisphosphate receptor type 3 (IP3R3)[27,28]. On the other hand, BBOX1 and carnitine metabolism were recently shown to suppress hepatocellular carcinoma tumor formation[29], highlighting divergent roles of BBOX1 in different types of cancer. However, the role of BBOX1 in other cancers such as kidney cancer is poorly understood.

In this work, we systematically characterize BBOX1 in human cancers and find that BBOX1 expression is often lost in ccRCC. BBOX1 is abundantly expressed in renal proximal convoluted tubule (PCT) cells, which are considered to give raise to ccRCC[30,31]. Our data shows that BBOX1 restoration inhibits cell viability and tumorigenesis in ccRCC xenograft models. Notably, its tumor-suppressive role is independent of carnitine metabolism. We find that BBOX1 antagonizes mTORC1 and glycolysis in physiological conditions through attenuating the DCLK2-TBK1 oncogenic signaling.

Results

BBOX1 is significantly downregulated in ccRCC

To systematically characterize the role of BBOX1 in human cancer, we performed a pan-cancer patient survival analysis on 33 types of human cancers by integrating data from the Cancer Genome Atlas (TCGA) associated with various genomic features of *BBOX1*, which included gene expression, DNA methylation, copy number alteration, and gene mutation[32] (Fig. 1a, Supplementary Table 1). Notably, *BBOX1* gene expression was most significantly associated with patient survival in kidney renal clear cell carcinoma (KIRC or ccRCC, $P < 0.001$) with its high expression predicting favorable clinical outcomes (Fig. 1a, b). BBOX1 high expression was also associated with favorable clinical outcomes in kidney renal papillary cell carcinoma (KIRP or pRCC, $P = 0.023$), or worse clinical outcomes in bladder cancer (BLCA, $P = 0.023$) (Fig. 1a, Supplementary Fig. 1a). In addition, BBOX1 methylation is strongly correlated with worse patient survival in low-grade glioma (LGG, $P < 0.001$) (Fig. 1a). No strong correlation between patient outcomes and copy numbers or gene mutations were found across various cancers. (Fig. 1a).

Subsequently, *BBOX1* mRNA levels were significantly reduced in primary tumors of ccRCC compared to normal kidney tissue from the TCGA dataset (Fig. 1c) or a patient dataset from UT Southwestern (UTSW) Kidney Cancer Program[33] (Supplementary Fig. 1b). Moreover, lower *BBOX1* expression correlated significantly with stage, grade, molecular subtype[34], and nodal metastasis status of ccRCC (Supplementary Fig. 1c–f). At the single-cell level, we utilized a ccRCC scRNAseq dataset[35] and observed that *BBOX1* gene is lower expressed in renal tumor cells than renal epithelial cells (Fig. 1d–f).

To further determine the BBOX1 protein levels, analysis from the Clinical Proteomic Tumor Analysis Consortium (CPTAC) dataset revealed that BBOX1 protein was also reduced in tumors (Fig. 1g), and we observed similar correlations with advanced stage and grade as for BBOX1 protein (Supplementary Fig. 1g, h) compared with normal kidney tissues. We then performed immunohistochemistry (IHC) staining in 39 paired primary tumor/normal ccRCC patient tissue samples. BBOX1 protein expression was reduced in tumors versus paired normal tissues (Fig. 1h, i) and negatively correlated with tumor grade (Fig. 1j). We obtained similar results in 20 pairs of samples by western blots (Fig. 1k, Supplementary Fig. 1i) or by real-time quantitative reverse-transcription PCR (qRT-PCR) (Supplementary Fig. 1j). Compared to BBOX1, two other carnitine biosynthesis enzymes, TMLHE (or BBOX2, paralogs of BBOX1) and ALDH9A1 (Supplementary Fig. 1k), were more modestly suppressed or unchanged (Fig. 1k, Supplementary Fig. 1i).

Intriguingly, BBOX1 expression is highly tissue context-dependent, reflected by its expression predominantly detected in kidney, while the other organs with relatively low or negative expression levels[36] (Supplementary Fig. 1l). In kidney, BBOX1 is predominantly expressed in renal proximal convoluted tubule (PCT) epithelial cells where ccRCC and pRCC derive from refs. 30,31 and is depleted in tumor cells (Fig. 1h, Supplementary Fig. 1m). Next, we examined BBOX1 expression in a panel of human RCC cell lines and renal PCT cells (RPTEC, HK-2, and HKC). In line with the observations in patient tumors, *BBOX1* mRNA and protein levels were reduced in most of the ccRCC cells except A704 (Fig. 1l, m), while the other genes in the carnitine biosynthesis pathway did not exhibit such pattern. We noticed that BBOX1 level in immortalized renal PCT cells (HK-2 and HKC) was similar as in ccRCC cell lines that was lower compared to primary RPTEC cells (Fig. 1l, m). We therefore hypothesized that BBOX1 might undergo selective silencing during malignant transformation. To this end, we transformed primary RPTEC cells by expressing either hTERT1 or SV40 large T antigen and examined the BBOX1 expression. We found a significant reduction of BBOX1 mRNA (Fig. 1n, Supplementary Fig. 1n) or protein levels (Fig. 1o, Supplementary Fig. 1o) in the transformed cells. In comparison, TMLHE, ALDH9A1, and SHMT1 were either unaffected or inconsistently changed (Fig. 1n, o, Supplementary Fig. 1n, o). Collectively, these analyses support the role of BBOX1 as a potential tumor suppressor in ccRCC.

BBOX1 suppresses ccRCC tumorigenesis in vivo

To investigate the functional roles of BBOX1 in ccRCC, we expressed BBOX1 ectopically in multiple ccRCC cells using stable expression (pLenti6 vector) or doxycycline (Dox)-inducible (pInducer) systems (Fig. 2a, Supplementary Fig. 2a). We found that BBOX1 restoration did not affect the in vitro colony formation or cell proliferation of ccRCC cells cultured in DMEM medium (Fig. 2b, Supplementary Fig. 2b, c). To assess whether BBOX1 affects tumor growth, we inoculated these cells subcutaneously in NOD SCID gamma (NSG) mice. BBOX1 restoration significantly inhibited xenograft tumor growth (Fig. 2c, d, Supplementary Fig. 2d–g). BBOX1 expression in these xenograft tumors was comparable to the levels observed in normal kidney tissues (Supplementary Fig. 2h). To validate the in vivo phenotype under more physiologically relevant conditions, we labeled 786-O cells expressing empty vector (EV) or BBOX1 with firefly luciferase and injected them orthotopically into the kidney of NSG mice. Like the subcutaneous growth, BBOX1 restoration inhibited kidney orthotopic tumor growth (Supplementary Fig. 2i, j). Consistent with the bioluminescence signal, tumors expressing BBOX1 displayed reduced tumor weight in the

https://doi.org/10.1038/s41467-025-56955-y

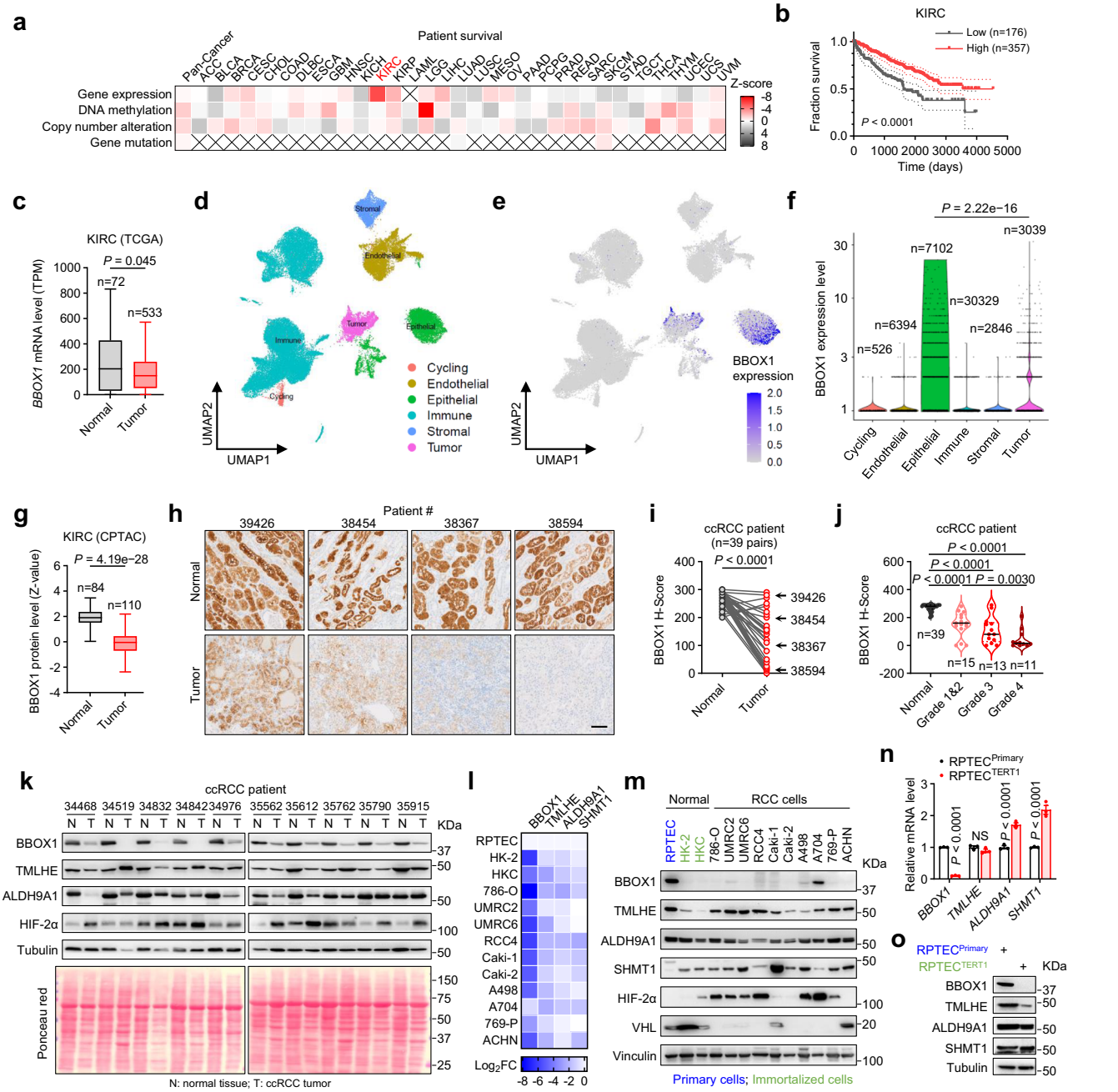

Fig. 1 | BBOX1 is significantly downregulated in ccRCC. a Comprehensive analysis of genetic features of *BBOX1* linked with cancer patient outcome in The Cancer Genome Atlas (TCGA). Z scores were calculated to indicate the directions of outcomes, Z score <0: favorable, red color, Z score >0: unfavorable, gray color. KIRC: Kidney Renal Clear Cell Carcinoma. Other TCGA cancer type abbreviations are listed in Supplementary Table 1. **b** The overall survival of patients with high/low BBOX1 expression in KIRC subtypes from the TCGA dataset. The number of patients is indicated. **c** *BBOX1* mRNA level of normal kidney tissues and primary tumor tissues in KIRC subtypes from the TCGA dataset. The number of patients is indicated. The median value (center line), lower quartile and upper quartile (box edges) and maximum and minimum value whiskers are indicated in the boxplot. Global single cell transcriptional map of ccRCC (**d**), and BBOX1 expression pattern from the RNA-seq of primary ccRCC tumors (**e**, **f**) obtained from Zvirblyte et al.[35]. Number of cells analyzed for each category: Cycling $n = 526$, Endothelial $n = 6394$, Epithelial $n = 7102$, Immune $n = 30329$, Stromal $n = 2846$, Tumor $n = 3039$. **g** BBOX1 expression level of ccRCC patients in normal kidney/primary tumor tissues in the CPTAC database. The median value (center line), lower quartile and upper quartile (box edges) and maximum and minimum value whiskers are indicated in the boxplot. Representative immunohistochemistry staining images of BBOX1 (**h**) and H-score quantification stratified by adjacent normal kidney/primary tumor tissues (**i**), or tumor grade (**j**) of 39 paired ccRCC patient samples. Scale bar, 100 μm. **k** Immunoblot analysis of BBOX1 protein level in 10 pairs of adjacent normal kidney/primary tumor tissues from ccRCC patients. A heatmap illustrated the $\log_2$ fold mRNA level quantified by qRT-PCR ($n = 3$ technical replicates) (**l**) and immunoblot (**m**) of BBOX1 and related carnitine synthesis enzymes in a panel of normal and RCC cells. qRT-PCR ($n = 3$ biological cell samples, this experiment has been performed twice with similar results) (**n**) and immunoblot (**o**) of BBOX1 and related carnitine synthesis enzymes expression level in primary or hTERT1 immortalized RPTEC cells. Statistical analysis was conducted by log-rank test (**b**) or two-tailed Student's *t* test (**c**, **f**, **g**, **j**, and **n**, unpaired; **i**, paired). Error bars represent SEM, NS denotes no significance. Representative immunoblots and gels shown in figures were repeated at least two times independently with similar results. Source data are provided as a Source Data file.

https://doi.org/10.1038/s41467-025-56955-y

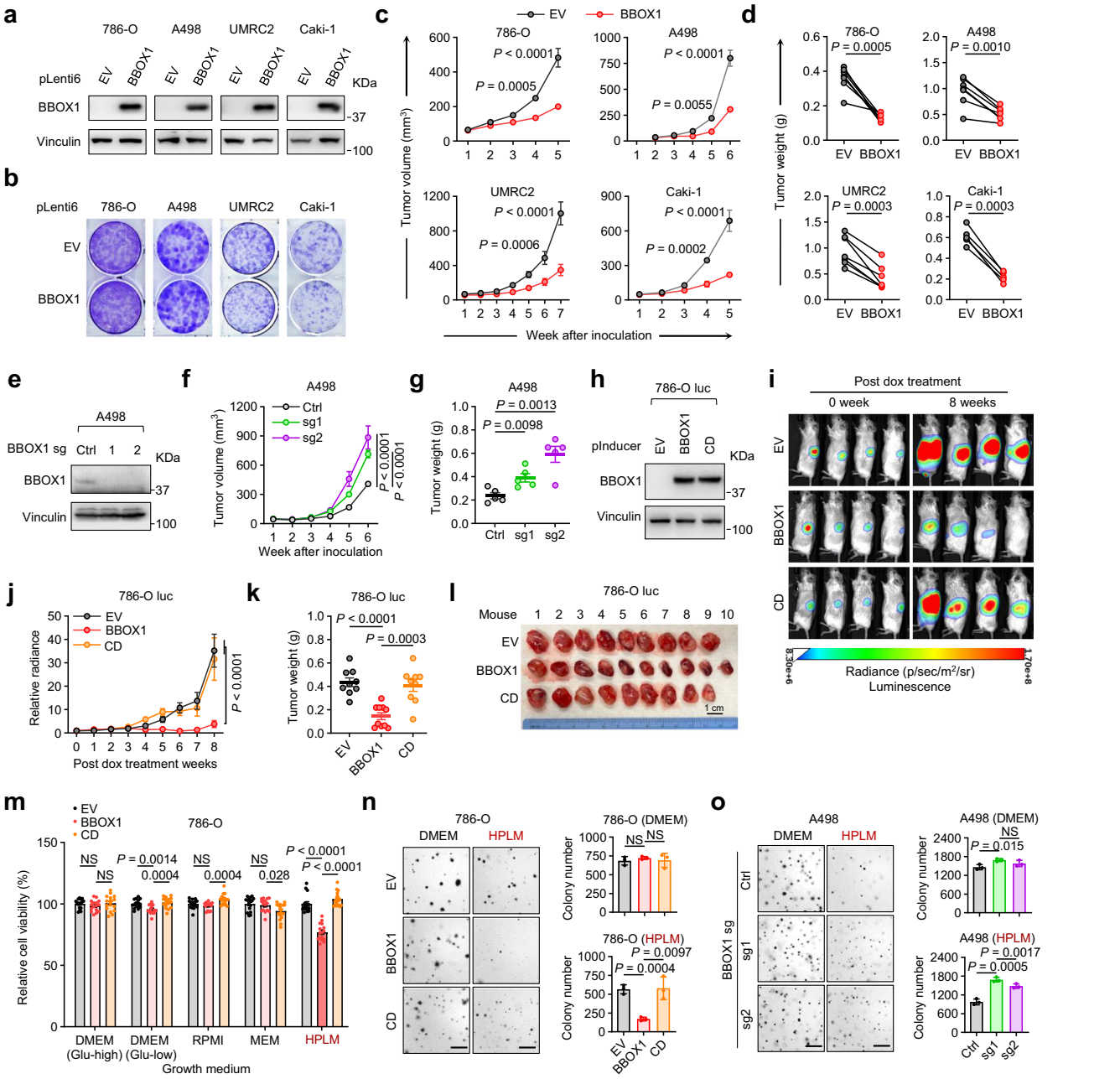

Fig. 2 | BBOX1 re-expression suppresses ccRCC tumorigenesis and cell growth in physiological growth conditions. a Immunoblots of BBOX1 re-expression in multiple ccRCC cell lines. Colony formation assay in DMEM (**b**), subcutaneous tumor growth (**c**), and tumor weight (**d**) of ccRCC cells expressing empty vector (EV) or BBOX1. 786-O, $n = 7$ mice; A498, $n = 7$ mice; UMRC2, $n = 7$ mice; Caki-1, $n = 5$ mice. Each mouse was inoculated with EV and BBOX1 cells at both flanks. Immunoblots of cell lysates (**e**), subcutaneous tumor growth (**f**), and tumor weight (**g**) of A498 cells with shRNA control (Ctrl) or BBOX1 depletion by two individual sgRNAs. Ctrl, $n = 5$ mice; sg1, $n = 5$ mice; sg2, $n = 5$ mice. Immunoblots of cells with doxycycline (dox) induction (**h**), representative bioluminescence images (**i**), corresponding quantification data (**j**), tumor weight (**k**), and image of tumors (**l**) from 786-O luciferase stable cells expressing EV, BBOX1, or catalytic dead (CD) mutant injected orthotopically into the kidney of NSG mice. EV, $n = 9$ mice; BBOX1, $n = 10$ mice; CD, $n = 9$ mice. **m** Relative cell viability of 786-O cells expressing EV, BBOX1, or CD mutant grown in different growth media. $n = 16$ independent cell cultures. This experiment has been repeated at least two times with similar results. Representative soft agar growth with colony quantifications of 786-O cells expressing EV, BBOX1, or CD mutant ($n = 3$ biological cell cultures) (**n**), or A498 cells expressing Ctrl, BBOX1 sg1 or sg2 ($n = 3$ biological cell cultures) (**o**) in indicated growth media. Each experiment has been repeated at least two times with similar results. Scale bar, 1 mm. Statistical analysis was conducted by two-way ANOVA followed by Tukey's multiple comparison test (**c**, **f**, and **j**) or two-tailed Student's *t* test (**d**, paired; **g**, **k**, and **m**–**o**, unpaired). Error bars represent SEM, NS denotes no significance. Representative immunoblots and gels shown in figures were repeated at least two times independently with similar results. Source data are provided as a Source Data file.

kidney (Supplementary Fig. 2k, l). We complemented overexpression experiments with loss of function studies. BBOX1 knockout by CRISPR-Cas9 or shRNA was sufficient to promote tumor growth in A498 (Fig. 2e–g) and A704 cells (Supplementary Fig. 2m–p).

Since BBOX1 is a metabolic enzyme with a known crystal structure[37], we then asked if the tumor suppressive function relied on its enzymatic activity. To this end, we generated a catalytic dead (CD) mutant of BBOX1 by substituting two conserved key residues (His-202,

Asp-204) in the active site to Ala, which is reported to completely block the enzymatic function of BBOX1[37–39]. We expressed CD mutant in 786-O cells along with wild type BBOX1. In contrast to the wild type, the CD mutant failed to suppress orthotopic or subcutaneous tumorigenesis (Fig. 2h–l, Supplementary Fig. 2q–t), suggesting that enzyme integrity of BBOX1 is critical for its tumor suppressive function. Altogether, these results show that BBOX1 suppresses ccRCC tumorigenesis in vivo.

BBOX1 inhibits ccRCC cell viability in physiological media due to limited glucose and/or glutamine level

Given the observation that BBOX1 restoration in ccRCC cells did not inhibit growth in vitro but reduced tumor growth in mice, and that the nutrient availability is considerably lower in mice than in traditional cell growth media[40], we hypothesized that limited nutritional availability may contribute to the in vivo phenotype. To test this notion, we grew 786-O or UMRC2 cells expressing EV, BBOX1, or CD mutant in various traditional media (DMEM, RPMI, or MEM, 10% serum) as well as in physiologic human plasma-like medium (HPLM, 10% serum)[41,42]. Different from the cells grown in the traditional media, ccRCC cells expressing wild type BBOX1 (but not CD mutant), had reduced viability in HPLM (Fig. 2m, Supplementary Fig. 3a, b). In addition, BBOX1 restoration in ccRCC cells dramatically reduced the anchorage-independent colony formation in soft agar assays in HPLM but not in DMEM media (Fig. 2n, Supplementary Fig. 3c–e). Conversely, BBOX1 knockout in A498 cells increased colony growth in HPLM soft agar (Fig. 2o).

Levels of glucose and glutamine, as well as other essential amino acids (methionine, leucine, and isoleucine), are much lower in HPLM than in DMEM or other traditional media (Supplementary Fig. 3f). To identify the specific nutrient(s) contributing to BBOX1 function, we performed 786-O cell viability assays in HPLM, supplemented with individual nutrient components to levels equivalent to those found in glucose-high DMEM. Supplementation with glucose and glutamine, but not methionine, leucine, or isoleucine, fully restored the reduced cell viability caused by BBOX1 restoration (Supplementary Fig. 3g). Furthermore, lower levels of glucose or glutamine were sufficient to abolish the phenotype of BBOX1 re-expression observed in HPLM (Supplementary Fig. 3h, i). To eliminate the potential effects of other nutrient components in HPLM, we cultured these cells in glucose- and glutamine-free DMEM. The viability of wild-type BBOX1-expressing cells phenocopied the HPLM medium but was abolished when glucose and glutamine were simultaneously added to the levels of HPLM or DMEM (Supplementary Fig. 3j). Interestingly, when glucose or glutamine was individually added, only high levels of glucose could rescue the cell viability of BBOX1-expressing cells (Supplementary Fig. 3j), suggesting that glucose plays a more important role than glutamine for mediating BBOX1 function.

BBOX1 suppresses ccRCC tumorigenesis independent of its canonical function

BBOX1 plays a tumor-suppressive role in hepatocellular carcinoma (HCC) through carnitine metabolism[29]. Given that catalytic integrity is critical for BBOX1 function (Fig. 2h–l, Supplementary Fig. 2q–t), we investigated whether BBOX1 suppresses ccRCC through its role in carnitine metabolism. We inoculated 786-O cells subcutaneously in NSG mice and when tumors reached ~50 mm^3, we administrated 4 mg/mL carnitine in the drinking water for 5 consecutive weeks (~20 mg/day). Carnitine treatment didn't suppress 786-O tumor growth (Supplementary Fig. 4a–c), although the serum and intertumoral carnitine levels were elevated in the treatment group (Supplementary Fig. 4d, e). In addition, 786-O, UMRC2, and A498 cells were treated with carnitine ranging from physiological level (~50 μM) to the levels that inhibiting in vitro cancer cell proliferation (2.5–10 mM)[43]. Carnitine treatment did not affect colony formation in ccRCC cells (Supplementary Fig. 4f), despite its demonstrated treatment efficacy with other cell lines[27].

We speculated that tumors in ccRCC or HCC respond differently to carnitine metabolism. BBOX1 loss decreases carnitine levels in HCC[44]. To determine whether this also occurs in ccRCC, we analyzed a metabolomics dataset from 138 patient ccRCC tumors and paired normal tissues[45]. We observed increased carnitine and its derivatives in tumors compared to normal tissues (e.g., carnitine, 1.3-fold, and acetylcarnitine, 2.8-fold; Supplementary Fig. 4g), suggesting that carnitine metabolism is not sufficient to suppress ccRCC. To further assess whether BBOX1 restoration affects carnitine metabolism in ccRCC tumor cells, we measured the abundance of carnitine and derivatives in the EV/BBOX1 expressing 786-O xenograft tumors as well as in vitro cells grown in DMEM medium. Intriguingly, carnitine levels did not change in 786-O xenograft tumors and only slightly increased in cells upon BBOX1 restoration (Supplementary Fig. 4h, i). Together, these results suggest that BBOX1 suppresses ccRCC independent of its canonical role in carnitine metabolism.

BBOX1 attenuates mTORC1 signaling in ccRCC

To elucidate the molecular mechanism by which BBOX1 suppresses ccRCC, we compared the transcriptomes of EV- and BBOX1-expressing 786-O xenograft tumors ($n = 3$ individual tumors) and their corresponding in vitro cells ($n = 3$ biological replicates) cultured in DMEM by RNA sequencing (RNA-seq). Principal component analysis (PCA) revealed that EV- and BBOX1-expressing cells had similar transcriptomic profiles while the EV tumors were separate from the BBOX1 tumors (Supplementary Fig. 5a). While there were few differentially expressed genes (DEGs) between EV and BBOX1 cells (105 upregulated and 305 downregulated, $p < 0.05$) (Supplementary Fig. 5b), there were significant transcriptome alterations between EV and BBOX1 tumors (1167 upregulated and 1330 downregulated DEGs, $p < 0.05$) (Supplementary Fig. 5c). Very few concordant DEGs were observed between the in vitro cells and in vivo xenograft tumors (Fig. 3a, b). Gene set enrichment analysis (GSEA) revealed cell cycle and metabolic pathways including MYC targets, hypoxia, E2F targets, G2M checkpoint, mTORC1 signaling, and glycolysis as the top gene sets that reduced in BBOX1 tumors (Fig. 3c, d, Supplementary Fig. 5d). In contrast, no such gene expression signatures were discovered by GSEA in cells grown in DMEM (Fig. 3e, f, Supplementary Fig. 5e). Gene ontology (GO) analysis further revealed downregulation of many metabolic pathways implicated in amino acid biosynthesis, carbon metabolism, and glycolysis in the BBOX1 tumors (Supplementary Fig. 5f). Similar to GSEA, very few of such metabolism related pathways were altered in these cells grown in vitro (Supplementary Fig. 5g).

It is known that mTORC1 plays a pivotal role in ccRCC and is hyperactivated in ccRCC tumors[20,21]. Moreover, mTORC1 functions as a central hub in regulating these metabolic pathways, including MYC pathway, hypoxia, and glycolysis[17–19]. Genes related to mTORC1 or downstream signaling were significantly downregulated in BBOX1-expressing tumors but not cells (Fig. 3g, Supplementary Fig. 5h). These results were further validated by qRT-PCR (Supplementary Fig. 5i). Activation of mTORC1 signaling in ccRCC was further suggested by the CPTAC datasets as well as our immunoblot and IHC analyses (Supplementary Fig. 6a–f). These results prompt us to investigate the potential regulation of mTORC1 signaling by BBOX1 in ccRCC under physiological conditions. mTORC1 activity, which is indicated by the phosphorylation status of its classical downstream targets including ribosomal protein S6 kinase (S6K1) and eukaryotic translation initiation factor 4E-binding protein 1 (4EBP1), was significantly reduced by BBOX1 restoration in various ccRCC xenograft tumors (Fig. 3h, i, and Supplementary Fig. 6g–i). By contrast, the protein level of IP3R3, an oncogenic protein whose level was regulated by BBOX1 in breast cancer[27,28], was not affected (Supplementary Fig. 6g–i). This result indicates that BBOX1 plays divergent roles in different cancer types.

https://doi.org/10.1038/s41467-025-56955-y

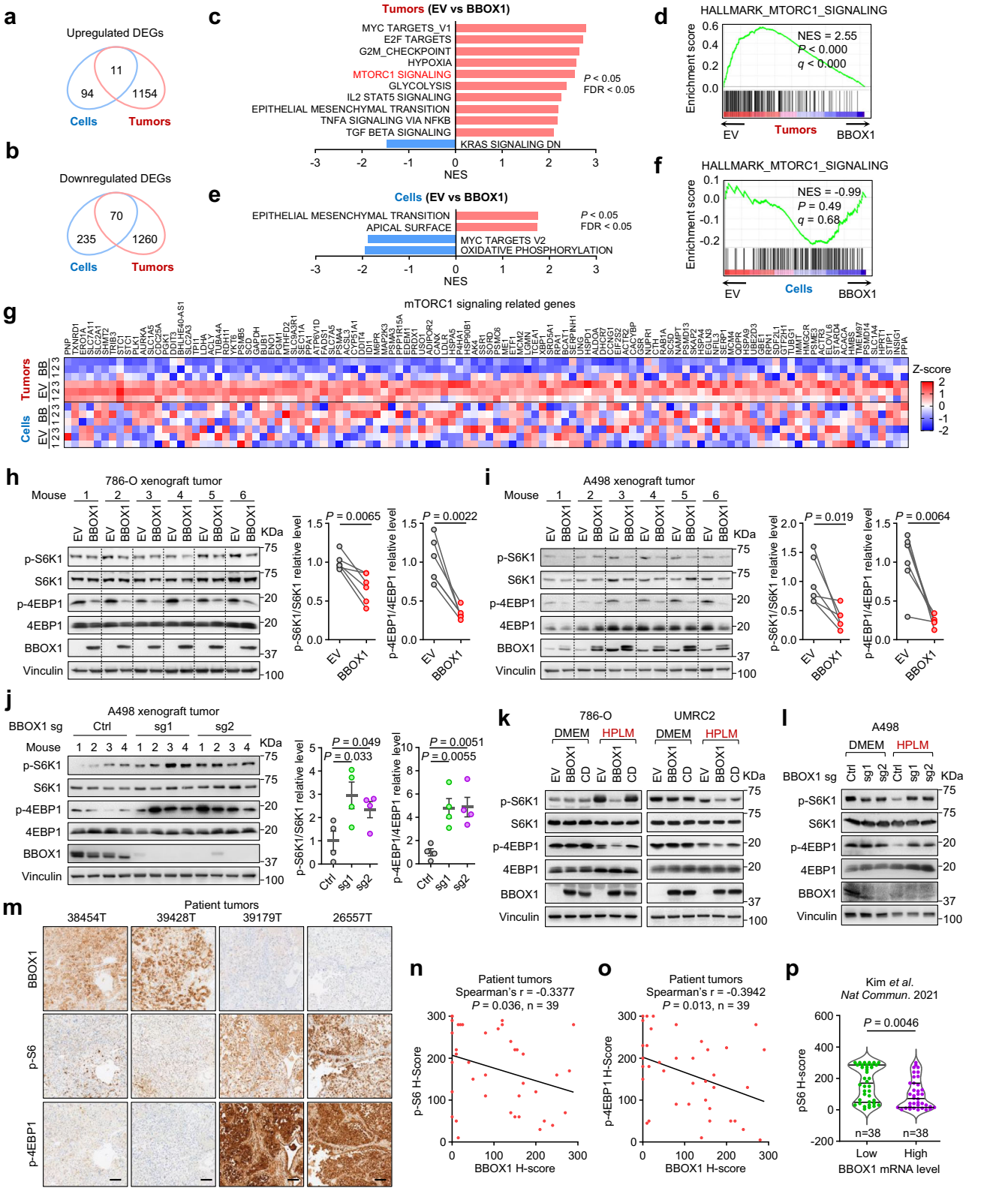

Conversely, BBOX1 depletion increased mTORC1 activity in A498 tumors (Fig. 3j). In addition, inhibition of mTORC1 signaling by BBOX1 restoration was further observed in ccRCC cells cultured in HPLM, but not DMEM medium, in an enzymatic dependent manner (Fig. 3k, Supplementary Fig. 6j). Knockout of BBOX1 in A498 cells also resulted in mTORC1 activation in HPLM (Fig. 3l). We observed increased mTORC1 activity in transformed RPTEC cells where BBOX1 expression was repressed compared to primary RPTEC cells (Supplementary Fig. 6k). To examine the relationship between BBOX1 level with mTORC1 activities in ccRCC patients, we conducted IHC staining with the 39 paired tumor/normal ccRCC patient samples for phospho-S6 and phospho-4EBP1. We found a statistically significant negative correlation between BBOX1 and mTORC1 signaling in patient tumors (Fig. 3m–o), and this correlation was further strengthened when combined with the normal tissues (Supplementary Fig. 6l–n). This finding was further validated in a secondary independent cohort of

Fig. 3 | BBOX1 attenuates mTORC1 signaling in ccRCC. Venn diagram for upregulated (**a**) or downregulated (**b**) differentially expressed genes (DEGs, BBOX1 vs EV log2FC > 0.5 or < −0.5, $P < 0.05$) in EV/BBOX1 786-O xenograft tumors or in vitro cells grown in DMEM. The number of unique or overlapped DEGs in each condition was indicated. **c**–**f** Gene set enrichment analysis (GSEA) using normalized gene expression values of EV or BBOX1 samples from 786-O xenograft tumors (**c**) or in vitro cells grown in DMEM (**e**), $n = 3$ biological replicate samples per group. Hallmark gene sets were used. Downregulated or upregulated signaling pathways with FDR < 0.05, $P < 0.05$ are shown. GSEA enrichment plot of the mTORC1 signaling from 786-O xenograft tumors (**d**) or in vitro cells grown in DMEM (**f**) were shown. NES, Normalized Enrichment Score. **g** Heatmap reveals gene expression of mTORC1 signaling related genes in EV/BBOX1 786-O xenograft tumors or in vitro cells grown in DMEM. $n = 3$ biological tumor or cell samples per group. Immunoblots and gel quantifications of tumor lysates from 786-O (**h**) or A498 (**i**) xenograft tumors expressing EV or BBOX1. $n = 6$ paired tumors, each mouse was inoculated with EV and BBOX1 cells at both flanks. **j** Immunoblots and gel quantifications of tumor lysates from A498 xenograft tumors expressing control sgRNA (Ctrl), or BBOX1 sgRNA 1 and 2. $n = 4$ mice. **k** Immunoblots of 786-O or UMRC2 cells expressing empty vector (EV), BBOX1, or catalytic dead (CD) mutant. **l** Immunoblots of A498 cells expressing Ctrl, or BBOX1 sgRNA 1 and 2. **m** Representative immunohistochemistry (IHC) staining images of BBOX1, phospho-S6 (at S240/244), and phospho-4EBP1 (at T37/46) in 39 ccRCC tumor samples. Scale bar, 100 μm. Spearman correlation between BBOX1 and phospho-S6 (**n**) or between BBOX1 and phospho-4EBP1 (**o**) in 39 ccRCC tumor tissues. **p** H-score of phosphor-S6 in ccRCC tumor thrombus samples stratified by low or high levels of BBOX1 mRNA expression from a previous study[46]. Two-tailed Student's *t* test (**h**, **i** paired and **j**, **n**–**p** unpaired), two-sided permutation test (**c**–**f**). Error bars represent SEM. Representative immunoblots and gels shown in figures were repeated at least two times independently with similar results. Source data are provided as a Source Data file.

ccRCC patients using samples obtained from ccRCC tumor extensions into the vasculature[46] (Fig. 3p). Collectively, these data suggest that BBOX1 suppresses mTORC1 signaling in ccRCC.

BBOX1 suppresses glycolysis in physiological conditions

ccRCC is characterized by enhanced glycolysis concomitant with repressed mitochondrial respiration, and glucose metabolism is particularly important for this type of malignancy[12–15]. Our RNA-seq data suggests that glycolysis is one of the top downregulated pathways in the BBOX1 expressing tumors (Fig. 3c, Supplementary Fig. 5f). Moreover, the other top downregulated signaling pathways, including mTORC1, MYC, and hypoxia (Fig. 3c), all playing critical roles in the induction of glycolysis[19,47,48]. Thus, we further assessed the regulation of the glycolytic pathway by BBOX1 in ccRCC. Like the mTORC1 signature, genes related to glycolysis were significantly downregulated in the 786-O xenograft tumors, but not cells cultured in DMEM medium (Fig. 4a). We further validated this phenomenon by examining the glycolytic genes by qRT-PCR. Most genes in the glycolytic pathway, such as those encoding glucose transporters (*GLUT1* and *GLUT3*), hexokinase 2 (*HK2*), and lactate dehydrogenase A (*LDHA*), were repressed by BBOX1 in vivo, but not in vitro (Fig. 4b, c). To interrogate the glucose utilization in tumors with BBOX1 expression, we performed stable isotope tracing by treating 786-O EV/BBOX1-expressing tumor bearing mice with [1,2-^{13}C]glucose. We then detected downstream metabolites derived from glucose (m + 2 isotopologues) in harvested tumors using liquid chromatography-mass spectrometry (LC-MS) (Fig. 4d). We observed an overall decrease in m + 2 enrichment of glycolytic intermediates in BBOX1 tumors (Fig. 4e). This was associated with decreased m + 2 enrichment of three TCA cycle intermediates (citrate, succinate, and malate) and amino acids (glutamate and aspartate) (Fig. 4f, g). Therefore, BBOX1 restoration potentially inhibits glycolysis in vivo.

We further performed seahorse experiments in 786-O or UMRC2 cells expressing EV/BBOX1 grown in DMEM or HLPM medium. Glycolytic rate and capacity were consistently decreased in BBOX1 re-expressing cells in HPLM as indicated by extracellular acidification rate (ECAR) (Fig. 4h, i). Likewise, BBOX1 knockout A498 cells increased the ECAR rate in HPLM, but not DMEM (Fig. 4j, k). Together, these results suggest that BBOX1 inhibits glycolysis in ccRCC.

TBK1 is the critical mediator that contributes to BBOX1 function in ccRCC

Next, to understand mechanistically how BBOX1 controls ccRCC tumorigenesis by suppressing mTORC1 and glycolysis, we used mass spectrometry to identify proteins that interact with BBOX1 in ccRCC tumors (Fig. 5a). Among the candidates showing at least a 2-fold enrichment ratio (BBOX1 vs. EV), 86 were overlapped in both models including TBK1, TANK, DNAJB11, RTF2, GPX1, and CAPZB (Fig. 5a, b, and Supplementary Data 1). We noticed that TBK1 (the top candidate) has been shown to regulate mTORC1[49–51], potentially linking BBOX1 and mTORC1 regulation. Thus, we focused on investigating TBK1 in mediating the function of BBOX1 in ccRCC. Subsequent immunoprecipitation revealed robust interactions between BBOX1 and TBK1, but not some other candidates, in ccRCC xenograft tumors (Fig. 5c, Supplementary Fig. 7a, b). Interestingly, this interaction appeared to be more pronounced in tumors compared to in vitro cells (Fig. 5d, Supplementary Fig. 7c). Of note, the CD mutant did not bind with TBK1 (Fig. 5d, Supplementary Fig. 7a–c). This observation aligns with the finding that CD mutant expression did not elicit a tumor-suppressive effect in ccRCC (Fig. 2h–l).

We then asked whether TBK1 is required for the tumor suppressive function of BBOX1 in ccRCC. In A498 cells grown in HPLM, we depleted TBK1 combined with BBOX1 knockout. The induced mTORC1 activity caused by BBOX1 knockout was blunted by concurrent TBK1 depletion (Fig. 5e). Likewise, the enhanced glycolytic activity in BBOX1 knockout cells was also abolished upon TBK1 depletion (Fig. 5f). We also conducted soft agar assays to assess the growth capacity of these cells in HPLM. The results showed that TBK1 depletion negated the growth-promoting effect elicited by BBOX1 knockout (Fig. 5g). We further evaluated tumorigenesis of these cells in NSG mice. BBOX1 knockout resulted in approximately a twofold increase in tumor growth, whereas TBK1 depletion remarkably inhibited tumor growth in both control and BBOX1 sgRNA cells (Fig. 5h, i, Supplementary Fig. 7d). On the other hand, compared with control cells, TBK1 knockdown by shRNA or sgRNA did not further inhibit mTORC1 activity caused by BBOX1 restoration in A498 or 786-O cells grown in HPLM (Fig. 5j, Supplementary Fig. 7e, f). Soft agar assays in HPLM and tumor growth validation further confirmed that the tumor suppressive role of BBOX1 was diminished by TBK1 depletion (Fig. 5k–m, Supplementary Fig. 7g). Taken together, these results indicate that TBK1 plays a critical role in BBOX1-dependent tumor suppression in ccRCC.

TBK1 is required for mTORC1 activation and glycolysis in physiological conditions

TBK1 has been shown to promote or inhibit mTORC1 in several cancer models[49–51], however, it remains unclear whether TBK1 regulates mTORC1 or other pro-tumorigenic pathways (like glycolysis) in ccRCC. We first validated the interaction between endogenous TBK1 and mTOR in A498 tumors or cells, which aligns with previous findings in other cancers[49,50]. This suggests that TBK1 may regulate mTORC1 activity through direct interaction in ccRCC (Fig. 5c, Supplementary Fig. 8a). We depleted TBK1 in 786-O or A498 cells using shRNA or sgRNA and examined mTORC1 signaling in DMEM and HPLM conditions. The mTORC1 activity was significantly repressed by TBK1 depletion only in HPLM but not in DMEM (Fig. 6a, Supplementary Fig. 8b). Pharmaceutical depletion of TBK1 by specific proteolysis targeting chimera (PROTAC)[52,53] led to a similar effect of mTORC1 repression in the HPLM condition (Fig. 6b). Contrarily, overexpressing

https://doi.org/10.1038/s41467-025-56955-y

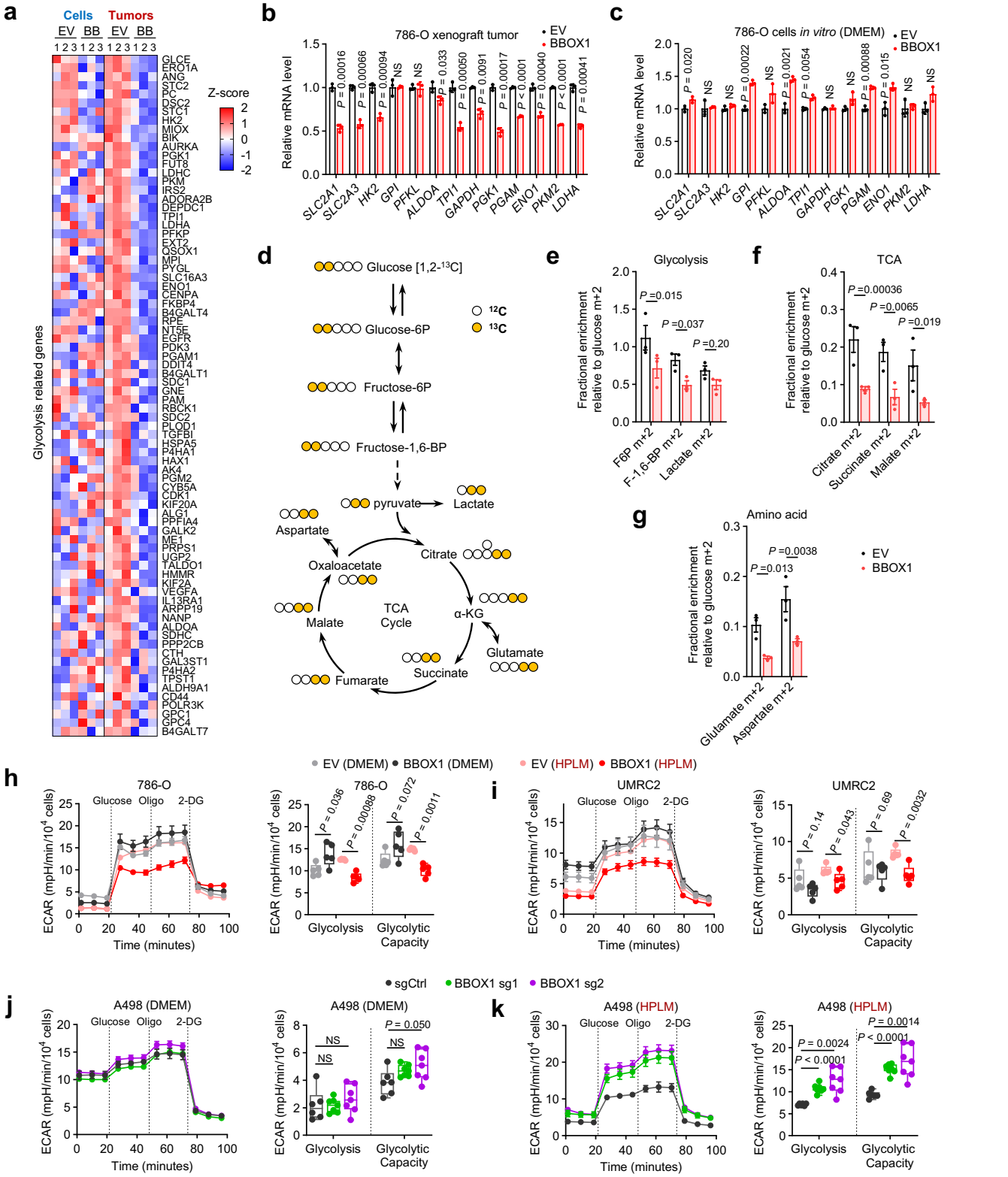

TBK1 or its phosphomimetic mutants S172D (the constitutive activate form of TBK1)[54] increased mTORC1 activity in ccRCC or HEK293T cells cultured in HPLM (Fig. 6c, Supplementary Fig. 8c, d). Therefore, these results suggest that TBK1 is necessary and sufficient for mTORC1 activation in ccRCC cells, specifically in physiological growth medium. To further assess whether TBK1 activates mTORC1 through its kinase activity, we treated 786-O cells with CMPD1, a selective TBK1 kinase inhibitor[55]. Notably, mTORC1 activity was reduced upon CMPD1 treatment in HPLM (Fig. 6d). As a control, CMPD1 treatment also resulted in a reduction in the Ser366 phosphorylation of p62, an established substrate of TBK1 in ccRCC[53], indicating a successful inhibition of the TBK1 kinase activity (Fig. 6d). We next examined the role of TBK1 in the glycolysis of ccRCC cells by seahorse. TBK1 depletion decreased glycolysis in A498 and 786-O cells in HPLM but not DMEM medium (Fig. 6e, Supplementary Fig. 8e, f), while TBK1 S172D overexpression increased glycolysis in HPLM (Fig. 6f).

Fig. 4 | BBOX1 suppresses glycolysis in physiological conditions. a Heatmap reveals gene expression of glycolysis related genes in 786-O xenograft tumors or in vitro cells grown in DMEM. $n = 3$ biological tumor or cell samples per group. qRT-PCR of glycolytic genes in EV/BBOX1 786-O xenograft tumors ($n = 3$ biological tumor samples per group) (**b**) or in vitro cells grown in DMEM ($n = 3$ biological cell samples per group) (**c**). Each experiment has been repeated two times with similar results. **d** Carbon flow of the isotopomer distribution of indicated metabolites derived from [1,2-^{13}C]glucose. M2 isotopomer distribution of indicated glycolytic metabolites (**e**), TCA cycle (**f**), and amino acids (**g**) in 786-O xenograft tumors with EV or BBOX1 expression. $n = 3$ biological tumor samples per group. Measurement of extracellular acidification rate (ECAR) in 786-O (**h**) or UMRC2 (**i**) cells expressing EV or BBOX1 grown in DMEM or HPLM medium. $n = 5$ independent cell cultures for each group. The median value (center line), lower quartile and upper quartile (box edges) and maximum and minimum value whiskers are indicated in the boxplot. Each experiment has been repeated two times with similar results. **j**, **k** Measurement of ECAR in A498 cells control sgRNA (Ctrl) ($n = 6$ independent cell cultures) or BBOX1 sgRNA 1 and 2 ($n = 7$ independent cell cultures) grown in DMEM (**j**) or HPLM (**k**) medium. The median value (center line), lower quartile and upper quartile (box edges) and maximum and minimum value whiskers are indicated in the boxplot. Each experiment has been repeated two times with similar results. Two-tailed Student's *t* test (**b**, **c**, **e**–**g**, and **h**–**k**, unpaired). Error bars represent SEM, NS denotes no significance. Source data are provided as a Source Data file.

We previously demonstrated that TBK1 depletion reduces cell proliferation under DMEM growth conditions by inhibiting the p62 signaling pathway[53]. Here we identified a role of TBK1 in sustaining mTORC1 activity and glycolysis in HPLM, indicating that TBK1 inhibition may provide additional growth inhibition under physiological conditions. We performed soft agar assays using A498 and UMRC2 cells with TBK1 shRNA expression in DMEM or HPLM media. TBK1 depletion diminished the 3D colony growth in DMEM, whereas this phenotype was further enhanced in the HPLM medium (Fig. 6g, Supplementary Fig. 8g).

To demonstrate that TBK1 controls mTORC1 and glycolysis in vivo, we subcutaneously inoculated A498 or UMRC2 cells with control or TBK1 shRNA. TBK1 depletion strongly inhibited ccRCC tumor growth in vivo (Fig. 6h, Supplementary Fig. 8h, i), which is in line with our previous study[53]. More importantly, mTORC1 activity was significantly reduced in xenograft tumors with TBK1 depletion (Fig. 6i, Supplementary Fig. 8j). We further found that the glycolytic genes in these tumors were significantly repressed after TBK1 depletion (Fig. 6j, Supplementary Fig. 8k). However, this phenomenon was abolished in the cells grown in DMEM (Fig. 6k, Supplementary Fig. 8l). Therefore, these results suggest that TBK1 promotes mTORC1 and glycolysis under physiological conditions, which are crucial for ccRCC tumorigenesis.

BBOX1 inhibits TBK1 activation through mitigating DCLK2-TBK1 interaction

Next, we examined how BBOX1 affects the TBK1 signaling in ccRCC. In BBOX1 restored ccRCC cells, TBK1 activity (indicated by Ser172 phosphorylation) was significantly reduced under physiological conditions (HPLM medium or xenograft tumors), while the total TBK1 protein levels remained unchanged. (Fig. 7a, b, Supplementary Fig. 9a–c). In contrast, BBOX1 knockout increased TBK1 phosphorylation under physiological conditions (Fig. 7c–e). Interestingly, TBK1 was activated in most of the ccRCC or immortalized PCT cells where BBOX1 expression was lost, and this phenomenon was reversed in primary RPTEC cells (Fig. 7f). Of note, BBOX1 silencing during RPTEC transformation is accompanied by TBK1 hypoactivation (Fig. 7g). We thus examine their correlation in patient samples. Immunoblotting of paired normal and tumor ccRCC samples revealed a strong negative correlation (20 out of 30 cases) between BBOX1 and TBK1 activities (Supplementary Fig. 9d). We further performed TBK1 and phosphor-TBK1 IHC staining in the aforementioned 39 ccRCC patient samples. Again, a negative correlation was found between BBOX1 and phospho-TBK1, but not TBK1 total proteins (Fig. 7h–j). Therefore, BBOX1 negatively regulates TBK1 activation in ccRCC.

We next examined potential mechanisms by which BBOX1 suppresses TBK1 activity. Although BBOX1 and TBK1 exhibited a strong interaction in ccRCC tumors or cells (Fig. 5c, d), GST-BBOX1 was unable to pull down in vitro translated TBK1 (Supplementary Fig. 9e), indicating that BBOX1 binds TBK1 indirectly, thereby ruling out the possibility that BBOX1 enzymatically modifies TBK1 activity. Previous research showed that TBK1 undergoes autophosphorylation at Ser172 through dimerization[56]. BBOX1 preferentially interacts with the ubiquitin-like domain and coiled-coil domain 1 (Supplementary Fig. 9f, g), which mediates TBK1 dimerization[56]. We wondered whether BBOX1 prevents TBK1 dimerization. Unexpectedly, our immunoprecipitation result indicated that BBOX1 facilitated the heterodimerization of Flag- and HA-tagged TBK1 in 293T cells (Supplementary Fig. 9h). We recently identified DCLK2 (especially the DCLK2-203 isoform) as a TBK1 activator in ccRCC[57]. We speculate that BBOX1 may function as an adaptor protein preventing DCLK2-TBK1 binding. Like TBK1, endogenous DCLK2-203 co-immunoprecipitated with wild type other than the CD mutant BBOX1 (Fig. 7k). Likewise, treating ccRCC cells with mildronate, a competitive inhibitor that binds to the substrate pocket of BBOX1[27,37], diminished the interaction between DCLK2 and BBOX1 (Fig. 7l, Supplementary Fig. 9i). However, TBK1 and BBOX1 interaction was not affected by BBOX1 inhibitor treatment (Fig. 7l, Supplementary Fig. 9i). This result suggests that DCLK2 may directly bind with BBOX1 by occupying its substrate pocket. We further confirmed their direct interaction by in vitro pulldown assays (Fig. 7m, Supplementary Fig. 9j). Interestingly, BBOX1 bound to DCLK2 at both the DCX1 and DCX2 domains (Supplementary Fig. 9k, l), the same regions where TBK1 also binds[57]. We thus hypothesize that BBOX1 may impair TBK1 activation by preventing DCLK2-TBK1 interaction. In 293T cells, the decreased binding between endogenous TBK1 and DCLK2-203 was associated with increased expression of BBOX1 (Fig. 7n), and this phenomenon was observed only in HPLM, not in DMEM medium (Supplementary Fig. 9m). Lastly, we performed in vitro kinase assays with in vitro translated (IVT) TBK1 mixed with ATP and recombinant DCLK2, the increased TBK1 phosphorylation by DCLK2 was diminished by recombinant BBOX1 (Fig. 7o). Intriguingly, mildronate abrogated this phenomenon (Fig. 7o), which aligns with the notion that BBOX1 inhibition mitigated BBOX1-DCLK2 interaction (Fig. 7l, Supplementary Fig. 9i), thereby inducing TBK1 activation.

Discussion

Our work identified BBOX1 as a previously uncharacterized tumor suppressor in ccRCC. Specifically, BBOX1 attenuated TBK1-mediated mTORC1 and glycolysis activation in physiological conditions. Mechanistically, BBOX1 inhibited TBK1 activation by antagonizing its upstream activator DCLK2 (Fig. 7p). Our study also indicated that the tumor-suppressive role of BBOX1 in ccRCC is independent of its canonical role in carnitine metabolism[23], which differs from a recent study in hepatocellular carcinoma[29]. In addition, our previous study revealed an oncogenic function of BBOX1 that doesn't rely on carnitine metabolism in triple negative breast cancer[27]. These studies suggest that BBOX1 plays multifaceted roles either dependent or independent of its canonical role in different types of malignancies. However, the function of BBOX1 in other types of cancer such as bladder cancer or glioma, whose prognosis data from patients significantly associated with BBOX1 gene features (Fig. 1a), is still unclear and warrants further investigation.

Although BBOX1 showed a tumor suppressive role in various ccRCC xenograft models, its function in a more rigorous physiological background like the genetic mouse with kidney BBOX1 conditional knockout is not clear, which is currently under investigation. Interestingly, BBOX1 exhibits tumor suppressive function in vivo but has no

https://doi.org/10.1038/s41467-025-56955-y

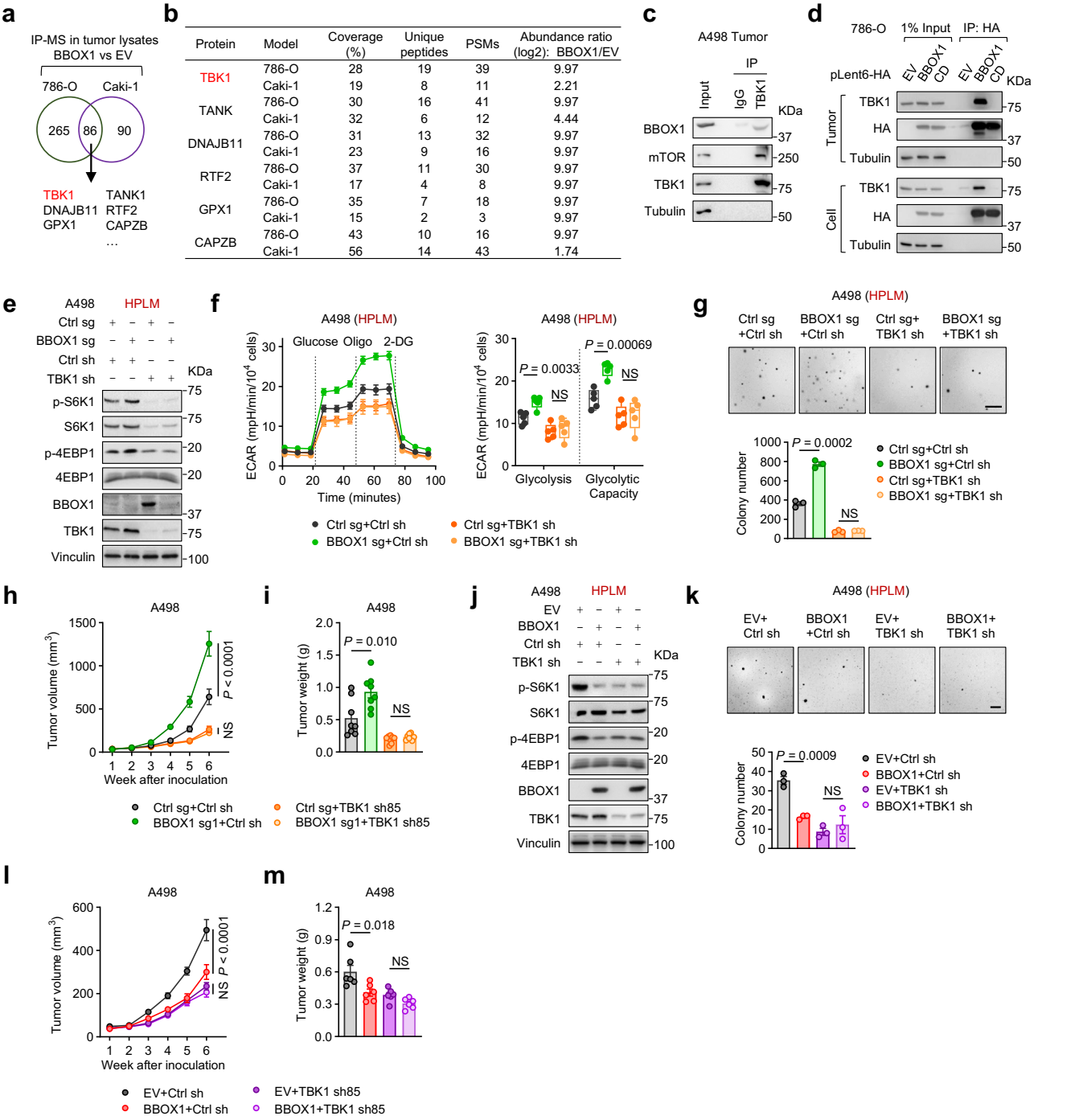

Fig. 5 | Identification of TBK1 as a key mediator contributing to BBOX1 function in ccRCC. a IP-mass spectrometry (MS) from 786-O and Caki-1 tumor lysates identified TBK1 as a top candidate protein interacting with BBOX1. **b** List of top BBOX1 binding proteins identified by IP-MS from 786-O and Caki-1 xenograft tumors. The full list of MS-identified proteins is provided in Supplementary Data 1. **c** Co-immunoprecipitation of endogenous TBK1 and endogenous BBOX1 in A498 xenograft tumors. **d** Co-immunoprecipitation of endogenous TBK1 and HA-tagged wild type BBOX1 or catalytic dead (CD) mutant in 786-O xenograft tumors or in vitro cells. **e**–**g** Immunoblots (**e**), ECAR measurement ($n = 5$ independent cell cultures, The median value (center line), lower quartile and upper quartile (box edges) and maximum and minimum value whiskers are indicated in the boxplot.) (**f**), and soft agar growth ($n = 3$ biological cell cultures) (**g**) of A498 cells expressing indicated BBOX1 sgRNA and TBK1 shRNA grown in HPLM medium. Each experiment has been repeated at least two times with similar results. Scale bar, 1 mm. **h**, **i** Subcutaneous xenograft tumor growth (**h**) and tumor weight (**i**) of A498 cells expressing indicated BBOX1 sgRNA and TBK1 shRNA. $n = 8$ mice for each group. Immunoblots (**j**) and soft agar growth ($n = 3$ biological cell cultures) (**k**) of A498 cells expressing indicated BBOX1 expression vector and TBK1 shRNA grown in HPLM medium. Each experiment has been repeated at least two times with similar results. Scale bar, 1 mm. Subcutaneous xenograft tumor growth (**l**), and tumor weight (**m**) of A498 cells expressing indicated BBOX1 expression vector and TBK1 shRNA. $n = 6$ mice for each group. Statistical analysis was conducted by two-way ANOVA followed by Tukey's multiple comparison test (**h** and **l**) or two-tailed Student's t test (**f**, **g**, **i**, **k**, and **m**). Error bars represent SEM, NS denotes no significance. Representative immunoblots and gels shown in figures were repeated at least two times independently with similar results. Source data are provided as a Source Data file.

https://doi.org/10.1038/s41467-025-56955-y

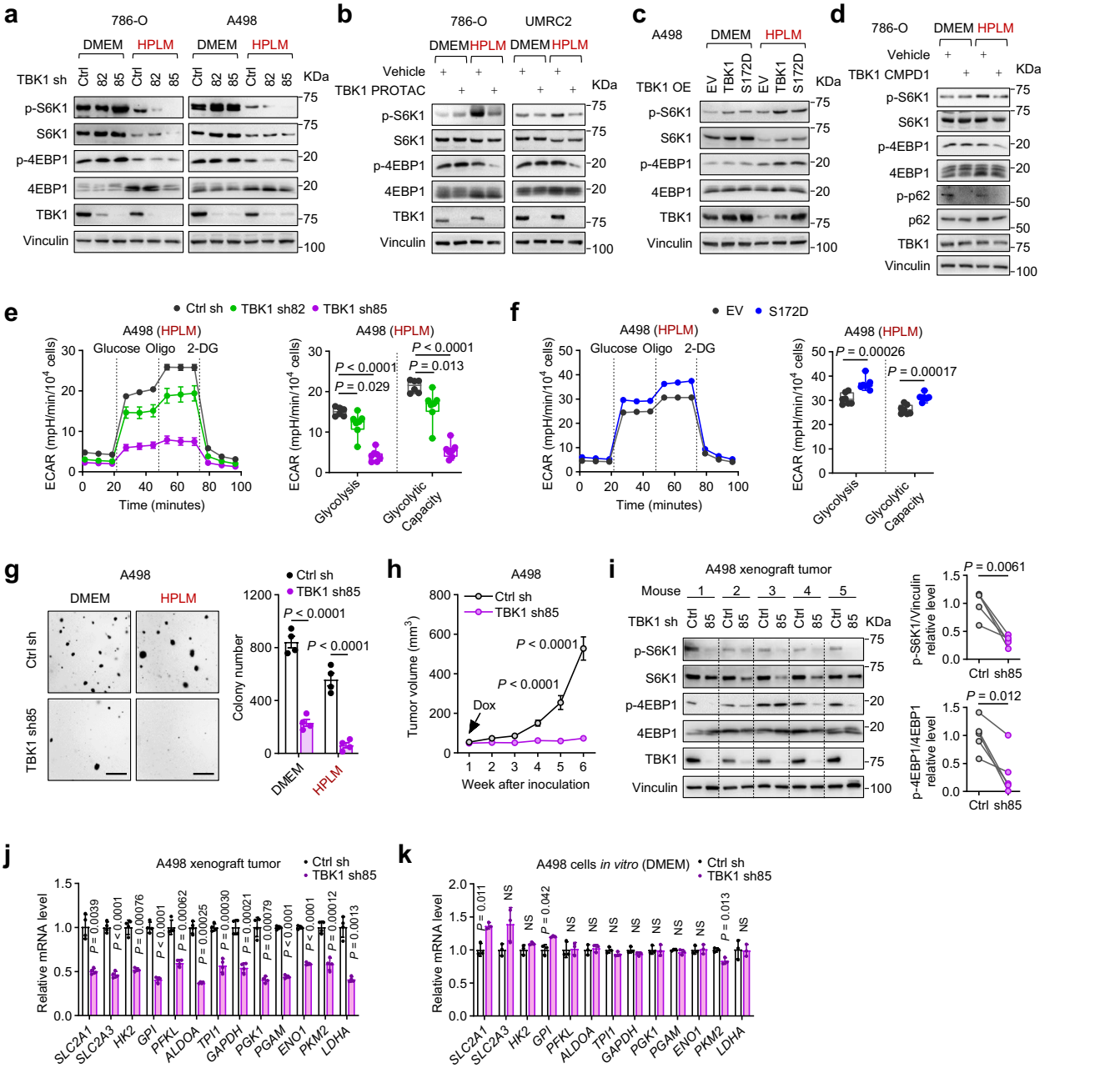

Fig. 6 | TBK1 is required for mTORC1 activation and glycolysis in physiological conditions. a Immunoblots of 786-O or A498 cells expressing doxycycline-inducible control shRNA (Ctrl), or TBK1 shRNAs (82, 85) grown in DMEM or HPLM medium. **b** Immunoblots of 786-O or UMRC2 cells treated with TBK1 PROTAC grown in DMEM or HPLM medium. **c** Immunoblots of A498 cells expressing empty vector (EV), wild type TBK1, or S172D mutant grown in DMEM or HPLM medium. **d** Immunoblots of 786-O cells treated with TBK1 CMPD1 grown in DMEM or HPLM medium. **e**, **f** Measurement of extracellular acidification rate (ECAR) in A498 cells expressing doxycycline-inducible control (Ctrl) ($n = 6$ independent cell cultures) or TBK1 shRNAs ($n = 7$ independent cell cultures) (**e**) or expressing EV, S172D mutant ($n = 7$ independent cell cultures for each group) (**f**) grown in HPLM. The median value (center line), lower quartile and upper quartile (box edges) and maximum and minimum value whiskers are indicated in the boxplot. Each experiment has been repeated two times with similar results. **g** Representative soft agar images (left) and colony quantification (right) of A498 cells expressing Ctrl or TBK1 shRNA 85 grown in DMEM or HPLM medium. $n = 4$ biological cell cultures for each group. This experiment has been repeated two times with similar results. Scale bar, 1 mm. Subcutaneous xenograft tumor growth ($n = 6$ mice for each group) (**h**), immunoblot with corresponding gel quantifications ($n = 6$ paired tumors, each mouse was inoculated with Ctrl and sh85 cells at both flanks) (**i**) of A498 cells with TBK1 depletion by shRNA 85. Doxycycline (Dox) chow was treated at the indicated time point. qRT-PCR of glycolytic genes in A498 xenograft tumors ($n = 4$ biological tumor samples per group) (**j**) or in vitro cells grown in DMEM ($n = 3$ biological cell samples per group) (**k**) expressing Ctrl, or TBK1 shRNA 85. Each experiment has been repeated two times with similar results. Statistical analysis was conducted by two-way ANOVA followed by Tukey's multiple comparison test (**h**) or two-tailed Student's *t* test (**e**, **f**, **g**, **j**, and **k**, unpaired; **i**, paired). Error bars represent SEM, NS denotes no significance. Representative immunoblots and gels shown in figures were repeated at least two times independently with similar results. Source data are provided as a Source Data file.

such effect on cells growth in traditional growth media. This phenomenon is similar to pVHL reintroduction which shows divergent phenotypes in 786-O cells in traditional in vitro growth or tumor formation in nude mice[58]. However, the mechanism by which BBOX1 suppresses tumorigenesis in vivo may be distinct from that of pVHL, which primarily functions through regulating cell cycle exit under physiological conditions with serum withdrawal[59]. Although we also observed a strong inhibition of cell cycle-related pathways

https://doi.org/10.1038/s41467-025-56955-y

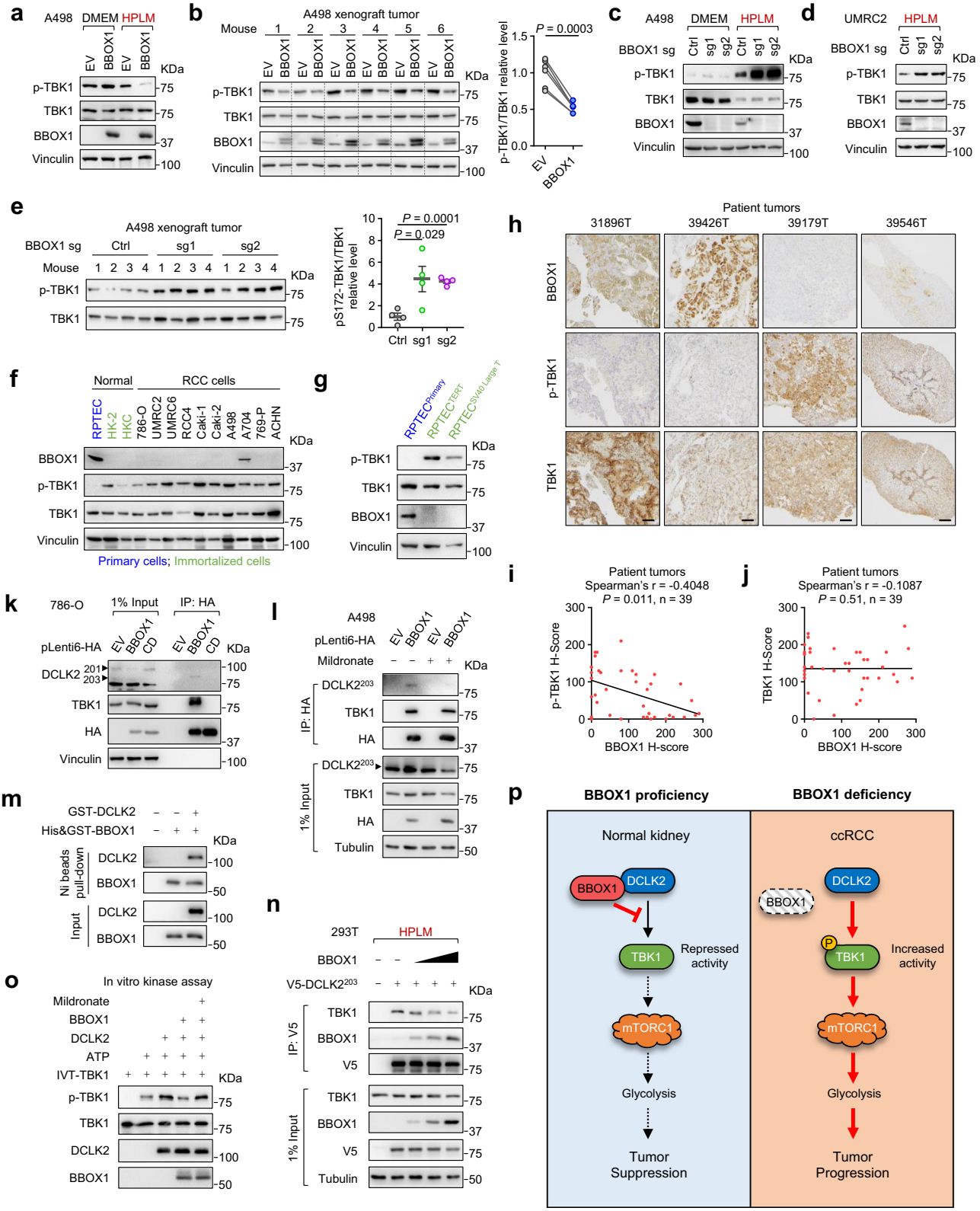

following BBOX1 restoration in ccRCC tumors (Fig. 3c), this effect is likely attributed to the downregulation of mTORC1, MYC, and HIF signaling. The fact that all growth media in our study were supplemented with 10% serum suggests that factors other than serum may be driving this phenomenon. We further pinpointed that glucose and/or glutamine may be the key nutrient(s) and their concentration determined the function of BBOX1. It is difficult to further interrogate the effect of glucose or glutamine individually due to their fundamental role and substantial overlapped downstream metabolism in supporting cell growth. Nevertheless, our data support the conclusion that inhibition of cellular metabolism, such as glycolysis, is a major reason for tumor suppression, and the presence of high levels of glucose and/or glutamine negates the tumor-suppressive role of BBOX1.

Importantly, we identified TBK1 as a critical BBOX1 downstream functional mediator in ccRCC. TBK1 is a serine/threonine-protein kinase involved in various cellular processes, including innate

Fig. 7 | BBOX1 negatively regulates TBK1 activation in ccRCC. Immunoblots of A498 cells expressing empty vector (EV) or BBOX1 grown in DMEM or HPLM medium (**a**) or xenograft tumors with quantifications ($n = 6$ paired tumors, each mouse was inoculated with EV and BBOX1 cells at both flanks) (**b**). Immunoblots of A498 (**c**) or UMRC2 (**d**) cells grown in DMEM or HPLM medium, or A498 xenograft tumors ($n = 4$ individual tumors for each group) (**e**) with BBOX1 knockout by sgRNAs. **f** Immunoblot of phospho-TBK1 and total TBK1 in various normal and RCC cells. **g** Immunoblot of phospho-TBK1 and total TBK1 in primary and transformed RPTEC cells. **h** Representative immunohistochemistry (IHC) staining images of BBOX1, phospho-TBK1 (at S172), and total TBK1 in 39 ccRCC tumor samples. Scale bar, 200 μm. Spearman correlation between BBOX1 and phospho-TBK1 (**i**) or between BBOX1 and TBK1 (**j**) in 39 ccRCC tumor tissues. **k** Immunoprecipitation of endogenous DCLK2, TBK1, and HA-tagged wild type BBOX1 or catalytic dead (CD) mutant in 786-O cells. Arrows indicate DCLK2 201 and 203 isoforms. **l** Immunoprecipitation of endogenous DCLK2-203 isoform, TBK1, and HA-tagged BBOX1 in A498 cells treated with 2 mM BBOX1 inhibitor for 72 h. **m** Pull-down assay between recombinant GST-DCLK2 and His-BBOX1 protein. **n** Immunoprecipitation of V5-tagged DCLK2-203 and endogenous TBK1 with increased expression of HA-tagged BBOX1 in 293T cells grown in HPLM medium for 48 h. **o** Immunoblots of in vitro kinase assay samples incubated with in vitro translated (IVT) TBK1, recombinant DCLK2 and BBOX1 proteins, ATP, or BBOX1 inhibitor (4 mM) as indicated. **p** Schematic model of the mechanism proposed for this study. Two-tailed Student's *t* test (**b**, paired; **e**, **l**, **j**, unpaired). Error bars represent SEM. Representative immunoblots and gels shown in figures were repeated at least two times independently with similar results. Source data are provided as a Source Data file.

immunity, autophagy, and cell growth regulation[60]. Recently, we elucidated its oncogenic role in VHL mutated kidney cancer by controlling p62 stability[53]. Although TBK1 was well documented in controlling the mTORC1 signaling in several malignancies, whether it activates or inhibits mTORC1 activities in cancer is under debate[49–51]. How TBK1 regulates mTORC1, especially under the physiological conditions in ccRCC is unclear. Our study showed that TBK1 is required to maintain the activities of mTORC1 and glycolysis in ccRCC. Intriguingly, BBOX1 interacts with TBK1 indirectly according to our in vitro pulldown assay, probably mediated by other adaptor proteins such as TANK (Supplementary Fig. 7a, b)[61]. Our mechanistic study revealed that BBOX1 regulates TBK1 activation by directly binding to DCLK2[57], thereby uncovering an important regulatory pathway for TBK1. It is worth mentioning that DCLK2 was not shown in the MS analysis due to its low abundance in ccRCC[57].

We show that the downregulation of BBOX1 is a common phenomenon in ccRCC. Unlike other common tumor suppressor genes such as *VHL*, *PBRM1*, *SETD2*, and *BAP1* whose loss of function is mainly caused by chromosome 3p loss[16]. The *BBOX1* gene is located on chromosome 11p, which is not a hotspot for chromatin mutations, indicating that genetic mutation is not the reason for BBOX1 loss of expression. Besides, the simultaneous downregulation of mRNA and protein levels of BBOX1 in ccRCC suggests that BBOX1 expression may be epigenetically or transcriptionally regulated. Importantly, we found that BBOX1 is selectively repressed during ccRCC malignant transformation, which is consistent with a recent finding for the leucyl-tRNA synthetase tumor suppressor[62]. However, the regulation of BBOX1 expression is enigmatic and needs further study. Overall, our current study reveals that BBOX1 functions as a tumor suppressor for ccRCC. As mTORC1 inhibition is a promising clinical treatment for patients with ccRCC. Therefore, our findings could guide novel therapeutic strategies, and BBOX1 could potentially serve as a biomarker for mTORC1 inhibition in ccRCC.

There are several limitations to the current study. We have not yet delineated the consequences of BBOX1 loss during ccRCC initiation. Future studies will assess *Bbox1* kidney conditional knockout (cKO) in genetically engineered mouse models along with *Vhl* cKO[63]. Additionally, the precise mechanism by which BBOX1 regulates TBK1 activity and ccRCC tumorigenesis preferentially in physiological conditions remains unclear. Whether BBOX1 specifically relies on certain nutrient intermediate(s) of glucose/glutamine metabolism to preserve its function needs further investigation. Lastly, additional downstream factors of BBOX1, such as HIF or MYC, that may attenuate the metabolic activity and tumorigenesis of ccRCC could exist. Identifying these factors will expand the role of BBOX1 in ccRCC biology and provide new therapeutic insights.

Methods

Ethical approval

The deidentified fresh-frozen human paired (ccRCC and adjacent normal tissue) samples used in this study were obtained from the UT Southwestern tissue management core, and have been reviewed by The UT Southwestern Human Research Protection Program (HRPP), which determined that the analysis does not meet the definition of human subject research under 45 CFR 46.102 and therefore does not require Institutional Review Boards (IRBs) approval or oversight. Informed consent was obtained from the ccRCC patients regarding the use of tissue samples. All animal experiments were conducted in accordance with the National Institutes of Health (NIH) guidelines and were approved by the Institutional Animal Care and Use Committee (IACUC) in the University of Texas Southwestern Medical Center (Protocol # 2019-102794).

Patient data analysis

Pan-cancer patient survival analysis and Kaplan–Meier plots in the indicated renal cell carcinoma cohorts (KIRC, KIRP, KICH) were conducted by web portal (https://survival.cshl.edu/) using the Cancer Genome Atlas Program (TCGA) data. Z score was calculated by using multivariate Cox proportional hazards model[32]. *P*-values were determined using a log-rank test. The mRNA and protein levels of BBOX1 in ccRCC patients were plotted from the UALCAN data analysis platform[64] based on the TCGA and CPTAC datasets, respectively.

Cell lines and cell culture

HEK293T, 786-O, A498, Caki-1, Caki-2, ACHN, and HK-2 cells were purchased from ATCC. UMRC2, UMRC6, and RCC4 cells were purchased from Sigma Aldrich. Primary RPECT cells were purchased from Lonza (CC-2553). A704 cells were a gift from Dr. Haifeng Yang from Thomas Jefferson University. HKC cells were a gift from Dr. W. Kimryn Rathmell from Vanderbilt University. hTERT immortalized RPTEC cells (ATCC, CRL-4031) were a gift from Dr. Peter Ly from UT Southwestern. SV40 Large T antigen transformed RPTEC cells were generated in the lab. 769-P cells were cultured in RPMI-1640 medium (Gibco, 11875119). A704 cells were cultured in Eagle's Minimum Essential Medium (MEM) (ATCC, 30-2003). RPTEC cells and HK-2 cells were cultured in Renal Epithelial Cell Growth Medium (REGM) (Lonza, CC-3190). All other cell lines were routinely grown in Dulbecco's Modified Eagle's Medium (DMEM) (Gibco, 11995073). For experiments conducted in physiological growth conditions, cells were seeded and cultured in the Human Plasma-Like Medium (HPLM) (Gibco, A4899101) for at least 72 h before the experiment. DMEM, RPMI-1640, MEM, and HPLM media were supplemented with 10% FBS (Gibco) and 1% penicillin/streptomycin (Gibco) before use. All cells were cultured at 37 °C with 5% CO_2. All cells were authenticated via short tandem repeat testing. Mycoplasma testing was routinely carried out with MycoAlert® PLUS Mycoplasma Detection Kit (Lonza, LT07-703) to ensure cells are mycoplasma free.

Antibodies and reagents

Antibodies used for Western Blot in this study included: rabbit anti-TBK1 (3504), rabbit anti-phospho-TBK1(Ser172) (5483), rabbit anti-HIF2α (7096), rabbit anti-HIF1α (3716S), rabbit anti-p70 S6 Kinase (9202), rabbit anti-phospho-p70 S6 Kinase (Thr389) (9234), rabbit

anti-phospho-p70 S6 Kinase (Thr421/Ser424) (9204), rabbit anti-4EBP1 (9644), rabbit anti-phospho-4EBP1 (Ser65) (9451), rabbit anti-phospho-4EBP1 (Thr37/46) (2855), rabbit anti-phospho-S6 Ribosomal Protein (Ser235/236) (4858), rabbit anti-phospho-S6 Ribosomal Protein (Ser240/244) (5364), rabbit anti-p62 (39749), rabbit anti-VHL (68547), rabbit anti-TANK (2141S), rabbit anti-GPX1 (3206), rabbit anti-HA tag (3724), rabbit anti-GST (2625), mouse anti-α-Tubulin (3873) were from Cell Signaling Technology. Mouse anti-Vinculin (V9131) was from Sigma-Aldrich. Rabbit anti-BBOX1 (ab171959) was from Abcam. Mouse anti β-actin (sc-47778) was from Santa Cruz. Rabbit Anti-TMLHE (16621-1-AP) was from Proteintech. Rabbit anti-DCLK2 (detect both 201 and 203 isoforms; PA5-106515) was from Thermo Fisher Scientific. Rabbit Anti-ALDH9A1 (A7875), rabbit Anti-SHMT1 (A12489), Rabbit Anti-G6PD (A1537) were from ABclonal. Rabbit anti-p62 phospho-Ser366 (AF7374) was from Affinity Biosciences. Mouse anti-IP3R3 (610312) was from BD Biosciences. HRP-linked goat anti-mouse secondary antibody (7076) and HRP-linked goat anti-rabbit secondary antibody (7074) were from Cell Signaling Technology. Antibodies used for IHC staining were mouse anti-BBOX1 (Sigma-Aldrich, HPA007600), rabbit anti-phospho-4EBP1 (Thr37/46) (Cell Signaling Technology, 2855), rabbit anti-phospho-S6 Ribosomal Protein (Ser240/244) (Cell Signaling Technology, 5364). Main reagents used are as below: soft agar assay staining reagent Iodonitrotetrazolium chloride (Sigma-Aldrich, I8377), MTS reagents (Abcam, ab197010), Crystal violet (Sigma-Aldrich, C-6158), Doxycycline (Sigma-Aldrich, D9891), D-Luciferin-potassium salt (Goldbio, LUCK), Ponceau S (Sigma-Aldrich, P3504). Mildronate (MedChem Express, HY-B1836), Recombinant human DCLK2 (SignalChem, D15-11G-10), Recombinant human BBOX1 (Sino Biological, 103663-196).

Western blot, immunoprecipitation, and pull-down assay

EBC buffer (50 mM Tris-HCl pH8.0, 120 mM NaCl, 0.5% NP40, 0.1 mM EDTA, and 10% glycerol) supplemented with complete protease inhibitor and phosphoSTOP tablets (Roche Applied Bioscience) was used as lysis buffer. Tissue samples were homogenized by using TissueRuptor II (QIAGEN) while cell samples were lysed directly in EBC buffer followed by centrifuging at 18,000 × *g*, 4 °C for 10 min using a benchtop centrifuge (MIKRO 200 R). Lysate concentration was measured by Protein assay dye (BioRad). Equal amount of cell lysates that equal to 20–40 mg of total proteins was resolved by SDS-PAGE for western blot analysis. For immunoprecipitation, lysates with equal amounts of proteins were incubated with indicated antibody conjugated beads for 6–8 h at 4 °C. After incubation, beads were washed with ice-cold EBC buffer three times, and bound protein complexes were eluted with SDS loading buffer and then subjected to western blot analysis. Anti-HA Affinity Matrix was from Roche (11815016001), Anti-FLAG M2 Affinity Gel (A2220) and Anti-V5 Agarose Affinity Gel (A7345) were from Millipore-Sigma. For the pull-down assay, in vitro translated (IVT) proteins using the T7 Quick Coupled Transcription/Translation System (Promega, L1170) were incubated with indicated recombinant protein overnight at 4 °C. Bound complexes were centrifuged, washed with EBC buffer, subjected to SDS-PAGE, and immunoblotted for the indicated antibodies.

In vitro kinase assay

In vitro kinase reaction was prepared by adding 3 µL in vitro translated TBK1 product with 1 µL 10 mmol/L ATP, 2 µL recombinant DCKL2, 1 µL recombinant BBOX1, or 4 mM (final concentration) mildronate as indicated in kinase reaction buffer (20 mmol/L Tris-HCl pH 7.4, 500 mmol/L β-glycerol phosphate, 12 mmol/L magnesium acetate) to reach a 30 µL reaction system. The reaction system was then incubated at 30 °C in an Eppendorf ThermoMixer C with 600 rpm for 1 h. Then 7.5 µL 5x SDS loading buffer was added to stop the reaction. After boiling at 95 °C, Western Blot was performed to detect indicated targets.

Cell viability assay

Cells were seeded in 96-well plates (500-1000 cells/well) in 100 µL of indicated growth medium supplemented with indicated nutrient components, the next day, 100 µL of additional such growth medium was added on the top. The 96-well plates were incubated at 37 °C with 5% CO_2 and kept monitored under the microscope for about 10 days until BBOX1 re-expressed cells started to die, MTS reagent was added in each well and cell viabilities were read at OD490 with a multi-plate reader.

Colony formation assay and soft agar growth

For colony formation assay, cells were seeded in duplicate in 6-well plates (1000 cells/well) after the cells reached a specific density visually, they were stained with 0.5% crystal violet for 1 h. For soft agar assay, 0.4% agar top layer containing specific numbers of cells (20,000 cells for DMEM medium and 30,000 cells for HPLM medium) was applied to 1% agar bottom layer. Add 0.5 mL medium after the top layer becomes solid then refresh the top liquid medium every 5 days. After 4–6 weeks, 100 µg/mL iodonitrotetrazoliuim chloride solution was used to stain cell colonies. Colony quantification was performed manually or by using ImageJ software.

RNA-seq

Total RNA from triplicates was extracted from homogenized xenograft tumors or in vitro cells grown in 6-well plates by using RNeasy® Mini Kit (QIAGEN, 74106) with on column DNase digestion (QIAGEN, 79256). Library preparation, sequencing, and data processing were performed by Novogen as paired end 100 bp reads. Gene set enrichment analysis (GSEA) was performed by using the GSEA software and Hallmark signatures. KEGG pathway enrichment analysis was performed by the DAVID functional annotation bioinformatics tools (https://david.ncifcrf.gov/home.jsp) using the up- or downregulated differentially expressed genes (DEGs). Z-scores are computed on a gene-by-gene (row-by-row) basis by subtracting the mean and then dividing by the standard deviation.

RT-qPCR

Total RNA was isolated with RNeasy mini kit with on column DNase digestion (Qiagen). First strand cDNA was generated with the iScript cDNA synthesis kit (BioRad). The resulting cDNA was diluted 1:20 with water for use in the qPCR analysis. qPCR was performed using iTaq Universal SYBR Green Supermix (BioRad) following the manufacturer's instructions. RT-qPCR primers used were listed in Supplementary Table 2.

IP-mass spectrometry analysis

Fresh frozen xenograft tumors (3 tumors per group from 786-O and Caki-1 xenograft expressing EV or BBOX1) were first combined and ground in liquid nitrogen using clean mortar and pestle, 200 mg of tissue samples were further homogenized in Lysis buffer (50 mM Tris-HCl pH7.5, 150 mM NaCl, 0.5% NP-40, 10% glycerol) using a handheld rotor-stator tissue Homogenizer (Qiagen) to obtain a final protein concentration (10 µg/µl). After centrifugation, equal amounts of tumor lysates were mixed with anti-HA antibody-conjugated beads (Roche Applied Bioscience) and incubated under rotation overnight at 4 °C. HA beads were washed with lysis buffer five times, and then HA-tagged proteins were eluted by incubating HA beads with 8 M urea buffer (200 mM Tris-HCl pH7.5, 100 mM NaCl) for 30 min at room temperature under constant rotation. Elution was performed three times. The final elution was filtered, then ice-cold 100% trichloroacetic acid (TCA) was added to the elution to obtain a final concentration of 20% TCA. After centrifugation at 4 °C at 20,000 × *g*, the pellet was washed with ice-cold 10% TCA once, then three times with ice-cold acetone. Every wash was followed by a 30-minute centrifugation at 4 °C at 20,000 × *g*. Finally, the pellet was

let air-dry at room temperature, and sent to mass spectrometry analysis. For mass spectrometry analysis, Protein pellets were resolubilized in 8 M urea, then each sample was reduced with 5 mM DTT, alkylated with 15 mM iodoacetamide, and digested with trypsin (Promega) overnight at 37 °C. The peptide samples were acidified to 0.1% TFA, desalted using C18 spin columns (Thermo) and dried via vacuum centrifugation. Each sample was analyzed in technical duplicate by LC-MS/MS using an Easy nLC 1200 coupled to a QExactive HF (Thermo Scientific). For data analysis, raw data files were processed using Proteome Discoverer version 2.5 (Thermo Scientific). Proteins were identified and quantified with Proteome Discoverer (v2.5) utilizing a Uniprot Human database (~20,000 proteins) appended with a common contaminants database. Log2 fold change ratios were calculated by subtracting the averaged log2 LFQ intensities of the BBOX1 re-expression samples from the averaged log2 LFQ intensities of the EV control samples.

Carnitine measurement

For carnitine in vivo treatment experiment, serum or intratumoral carnitine level was measured using an L-carnitine assay kit (Abcam, ab83392) followed by manufacturer's instructions. To determine levels of carnitine and its derivates in xenograft tumor tissues or in vitro cells, metabolites were extracted from equal amounts of homogenized tissues or cells using ice-cold methanol/water 80:20 (v/v) solution. Centrifuged supernatants were subjected to LC-MS analysis as previously described[65].

Seahorse XF ECAR measurement

The extracellular acidification rate (ECAR) was measured by an XFe24 extracellular flux analyzer (Agilent Technologies), according to the manufacturer's instructions. Briefly, cells were cultured in indicated medium for at least 72 h, then a total of 2×10^4 cells were seeded with 300 µl of the same medium into XF24 cell culture microplate 8 hrs before the assay. On the day following cell seeding, medium was changed to phenol red-free, Seahorse XF DMEM medium, pH 7.4 (Agilent Technologies) supplemented with 2 mM glutamine. Cells were equilibrated within 1 h in 37 °C incubator without CO_2. The basal extracellular acidification rate was first measured. Then the ECAR trace was recorded in response to sequential addition of indicated compounds from the Glycolysis Stress Test Kit (Agilent Technologies, 103020-100). The concentration of compounds used were glucose (10 mM), oligomycin (1 µM), and 2-DG (50 mM). 5–7 technical replicates were utilized per sample to calculate ECAR. The ECAR values were normalized to the average cell number in each well.

In vivo isotope tracing

Six-week old male NOD SCID Gamma mice (NSG, Jackson lab) were injected with 1×10^6 viable 786-O cells expressing EV or BBOX1 subcutaneously. Upon tumor establishment (~1000 mm^3), mice were fasted for 6 h before the tracing experiment. The in vivo isotope tracing experiment was described previously[65]. Briefly, [1,2,^{13}C]-glucose (Cambridge Isotope Laboratories) was dissolved in sterilized saline (20%, w/v). 100 µL of such [1,2,^{13}C]-glucose solution was injected 3 times with 15-minute interval into the tail vein. Mice were laying on 37 °C heat pad under anesthesia during the injection. Mice were then euthanized via cervical dislocation at 45 min after the first injection. Tumor tissue was rapidly harvested and snap frozen in liquid nitrogen and stored at −80 °C until analysis. For metabolites extraction, tumor tissues were first grinded in liquid nitrogen using clean mortar and pestle, ~30 mg of tumor tissue was added into 400 µL of ice-cold methanol/water 80:20 (v/v). The tissue was then homogenized using handheld rotor-stator tissue Homogenizer (Qiagen) and freeze-thawed for three cycles. After vortex rigorously for 1 min, the samples were centrifuged at ~20,160 × *g* for 15 min at 4 °C and the metabolite-containing supernatants were transferred into a new tube. Perform protein quantitation on the supernatant and transfer a volume equivalent to 10 µg of protein to a new Eppendorf tube. Finally, the tubes were speed vacuum dried at room temperature and then stored dry pellet in −80 °C freezer for further LC-MS analysis.

Immunohistochemistry (IHC)

The IHC staining was carried out by UT Southwestern Medical Center Tissue Management Shared Resource Core. Briefly, the slides were baked for 20 min at 60 °C, then deparaffinized and hydrated before the antigen retrieval step. Heat-induced antigen retrieval was performed at pH 9.0 for 20 minutes in a Dako PT Link. The tissue was incubated with a peroxidase block and then an antibody incubation (BBOX1, 1:100, 20 min; phospho-4EBP1 (Thr37/46), 1:400, 60 min; phospho-S6 Ribosomal Protein (Ser240/244),1:400, 60 min; Phospho-TBK1 (Ser172), 1:100, 45 min; TBK1, 1:100, 30 min). Antibody detection was performed using the Bond Intense R detection system (DS9263) with ImmPress HRP anti-rabbit or anti-mouse IgG (Vector Laboratories, MP-7451/MP-7402). Stained slides were dehydrated and coverslipped. Positive and negative controls (no primary antibody) were included during the run. For imaging analysis, stained slides were digitally scanned at 40x magnification using Aperio ScanScope-XT (Aperio Technologies, Vista, CA). All slides were read by a kidney pathologist from the Department of Pathology at UT Southwestern Medical Center. H Scores were calculated using the following formula: 3× percentage of strongly staining cells + 2× percentage of moderately staining cells + 1× percentage of weakly staining cells, giving a range of 0–300.

Animal studies

6–8-week-old NSG mice (Jackson Laboratories) were used for xenograft studies. For each xenograft tumor growth studies, male to female mouse ratio is set at 2:1 to mirror the human kidney cancer population[66]. For orthotopic kidney tumor growth, approximately 5×10^5 viable luciferase reporter expressed 786-O cells were resuspended in 20 µL PBS containing 50% matrigel (Corning, 354234) and injected orthotopically into the left kidney of each mouse. To monitor orthotopic tumor growth, mice were intraperitoneal injected at 150 mg/kg with the 15 mg/ml stock of D-Luciferin (Goldbio, LUCK-1G), and the bioluminescence signal was monitored weekly under a spectral AMI-HTX imaging system. For subcutaneous tumor growth, 1×10^6 viable cells (resuspended in 100 µL PBS containing 50% matrigel) in both flanks unless otherwise indicated in the figure legend. Tumor size was measured with digital calipers once a week and tumor volume was calculated as V = (L × W^2)/2, where L is the tumor length and W is the tumor width measured in millimeters. To induce BBOX1 expression or TBK1 shRNA expression, mice were fed with purina rodent chow #5001 with 2000ppm doxycycline (Research Diets, C11300-2000i) at indicated time in the figure legend. The maximal tumor burden permitted by ethics committee was no more than 2 cm for single tumor or cumulative diameter of 3 cm for multiple tumors, and the maximal tumor burden did not exceed the limit. Mice were housed in the ARC Mouse Facility at UT Southwestern under Specific-pathogen-free (SPF) conditions with climate control and 12-h light/dark cycles. Standard rodent diet and fresh water were provided continuously through an automated water system.

sgRNA and shRNA sequence

sgRNA targeting BBOX1 or TBK1 were selected by CRISPick (Broad Institute). The guide RNAs were cloned into pLentiCRISPR-v2-Puro or pLentiGuide-Puro vectors. shRNA targeting BBOX1 or TBK1 was described previously[27,53]. All sgRNA and shRNA sequences are listed in Supplementary Table 3.

Plasmids

Quick Change XL Site-Directed Mutagenesis Kit (Agilent Technologies, 200516) was used to construct catalytic dead (CD) mutant of BBOX1

(His-202, Asp-204 were substituted to Ala) and TBK1 S172D mutants. pcDNA-3.1-Flag-BBOX1, pcDNA-3.1-Flag-CD, pLenti6-HA-BBOX1, pLenti6-HA-BBOX1-CD were constructed using standard molecular biology techniques. pINDUCER-BBOX1/CD was constructed using the Gateway BP/LR clonase system (Invitrogen, 11789013/11791019) followed by the manufacturer's instructions. Other TBK1 or DCLK2-related plasmids were described in previous study[57]. All plasmids were sequenced to confirm validity.

Virus production and infection

HEK293T cells were used for generating lentivirus particles. Virus packaging plasmids were transfected with lipofectamine 3000 (Invitrogen). 8–12 h post-transfection, fresh medium was added to replace the old medium. Then, viruses were collected twice after 24 and 48 h. After passing through 0.45 μm filters, an appropriate amount of viruses was used to infect target cells in the presence of 8 μg/mL polybrene (Santa Cruz). Subsequently, target cell lines were cultured in the presence of puromycin (2 μg/ml) or neomycin (0.8 mg/ml) depending on the vector.

Statistics and reproducibility

Log-rank test was used for patient survival analysis. Two-way ANOVA followed by Tukey's multiple comparison test was used for all tumor growth studies. As indicated in figure legends, the unpaired or paired two-tailed Student's *t* test was used for experiments comparing two or multiple sets of data as indicated in the figure legends. All graphs depict mean ± SEM unless otherwise indicated. Graphs and statistics were generated by GraphPad Prism (10.1.2). NS denotes no significance. All experiments presented in the manuscript were repeated in at least two independent experiments or biological replicates with similar results.

Reporting summary

Further information on research design is available in the Nature Portfolio Reporting Summary linked to this article.

Data availability

Raw and processed RNA-seq data generated in this study have been deposited to the Gene Expression Omnibus (GEO) under accession GSE261401. The IP-mass spectrometry proteomics data generated in this study have been deposited to the ProteomeXchange Consortium via the PRIDE partner repository with the dataset identifier PXD050455. The processed IP-mass spectrometry proteomics data are provided in the Supplementary Data 1. The public metabolism datasets that have been reused in this study showing in Supplementary Fig. 4g can be found in the Supplemental Information (Table S2) of the referenced study (PMID: 26766592)[45]. The public IHC image was adopted from the Human Protein Atlas (Staining ID: HPA007600; URL: https://www.proteinatlas.org/ENSG00000129151-BBOX1/tissue/kidney#img). Image available from v24.0.proteinatlas.org. All the other data supporting the findings of this study are available within the article and its supplementary information files and source data. Source data are provided with this paper.

References

1. Siegel, R. L., Miller, K. D., Fuchs, H. E. & Jemal, A. Cancer statistics, 2022. *CA Cancer J. Clin.* **72**, 7–33 (2022).
2. Godwin, J. L., Zibelman, M., Plimack, E. R. & Geynisman, D. M. Immune checkpoint blockade as a novel immunotherapeutic strategy for renal cell carcinoma: a review of clinical trials. *Discov. Med.* **18**, 341–350 (2014).
3. Kaelin, W. G. Jr. Molecular basis of the VHL hereditary cancer syndrome. *Nat. Rev. Cancer* **2**, 673–682 (2002).
4. Kondo, K., Kim, W. Y., Lechpammer, M. & Kaelin, W. G. Jr. Inhibition of HIF2alpha is sufficient to suppress pVHL-defective tumor growth. *PLoS Biol.* **1**, E83 (2003).
5. Cho, H. et al. On-Target Efficacy of a HIF2alpha Antagonist in Preclinical Kidney Cancer Models. *Nature*, https://doi.org/10.1038/nature19795 (2016).
6. Chen, W. et al. Targeting Renal Cell Carcinoma with a HIF-2 antagonist. *Nature*, https://doi.org/10.1038/nature19796 (2016).
7. Courtney, K. D. et al. Phase I Dose-Escalation Trial of PT2385, a First-in-Class Hypoxia-Inducible Factor-2alpha Antagonist in Patients With Previously Treated Advanced Clear Cell Renal Cell Carcinoma. *J. Clin. Oncol.* **36**, 867–874 (2018).
8. Choueiri, T. K. et al. Inhibition of hypoxia-inducible factor-2alpha in renal cell carcinoma with belzutifan: a phase 1 trial and biomarker analysis. *Nat. Med.* **27**, 802–805 (2021).
9. Wettersten, H. I., Aboud, O. A., Lara, P. N. Jr. & Weiss, R. H. Metabolic reprogramming in clear cell renal cell carcinoma. *Nat. Rev. Nephrol.* **13**, 410–419 (2017).
10. Linehan, W. M., Srinivasan, R. & Schmidt, L. S. The genetic basis of kidney cancer: a metabolic disease. *Nat. Rev. Urol.* **7**, 277–285 (2010).
11. Sanchez, D. J. & Simon, M. C. Genetic and metabolic hallmarks of clear cell renal cell carcinoma. *Biochim. Biophys. Acta Rev. Cancer* **1870**, 23–31 (2018).
12. Courtney, K. D. et al. Isotope Tracing of Human Clear Cell Renal Cell Carcinomas Demonstrates Suppressed Glucose Oxidation In Vivo. *Cell Metab.* **28**, 793–800. e792 (2018).
13. Nilsson, H. et al. Primary clear cell renal carcinoma cells display minimal mitochondrial respiratory capacity resulting in pronounced sensitivity to glycolytic inhibition by 3-Bromopyruvate. *Cell Death Dis.* **6**, e1585 (2015).
14. Zhu, H., Wang, X., Lu, S. & Ou, K. Metabolic reprogramming of clear cell renal cell carcinoma. *Front. Endocrinol.* **14**, 1195500 (2023).
15. Rathmell, W. K., Rathmell, J. C. & Linehan, W. M. Metabolic Pathways in Kidney Cancer: Current Therapies and Future Directions. *J. Clin. Oncol.*, JCO2018792309, https://doi.org/10.1200/JCO.2018.79.2309 (2018).
16. Cancer Genome Atlas Research, N. Comprehensive molecular characterization of clear cell renal cell carcinoma. *Nature* **499**, 43–49 (2013).
17. Laplante, M. & Sabatini, D. M. mTOR signaling in growth control and disease. *Cell* **149**, 274–293 (2012).
18. Ben-Sahra, I. & Manning, B. D. mTORC1 signaling and the metabolic control of cell growth. *Curr. Opin. Cell Biol.* **45**, 72–82 (2017).
19. Mossmann, D., Park, S. & Hall, M. N. mTOR signalling and cellular metabolism are mutual determinants in cancer. *Nat. Rev. Cancer* **18**, 744–757 (2018).
20. Pantuck, A. J. et al. Prognostic relevance of the mTOR pathway in renal cell carcinoma: implications for molecular patient selection for targeted therapy. *Cancer* **109**, 2257–2267 (2007).
21. Robb, V. A., Karbowniczek, M., Klein-Szanto, A. J. & Henske, E. P. Activation of the mTOR signaling pathway in renal clear cell carcinoma. *J. Urol.* **177**, 346–352 (2007).
22. Kucejova, B. et al. Uncoupling hypoxia signaling from oxygen sensing in the liver results in hypoketotic hypoglycemic death. *Oncogene* **30**, 2147–2160 (2011).
23. Paul, H. S., Sekas, G. & Adibi, S. A. Carnitine biosynthesis in hepatic peroxisomes. Demonstration of gamma-butyrobetaine hydroxylase activity. *Eur. J. Biochem.* **203**, 599–605 (1992).
24. Bremer, J. Carnitine-metabolism and functions. *Physiol. Rev.* **63**, 1420–1480 (1983).
25. Dawany, N. B., Dampier, W. N. & Tozeren, A. Large-scale integration of microarray data reveals genes and pathways common to multiple cancer types. *Int. J. Cancer* **128**, 2881–2891 (2011).
26. Kim, K. S. et al. Low gamma-butyrobetaine dioxygenase (BBOX1) expression as a prognostic biomarker in patients with clear cell renal cell carcinoma: a machine learning approach. *J. Pathol. Clin. Res.* **9**, 236–248 (2023).

27. Liao, C. et al. Identification of BBOX1 as a Therapeutic Target in Triple-Negative Breast Cancer. *Cancer Discov.* **10**, 1706–1721 (2020).
28. Liao, C. & Zhang, Q. BBOX1 promotes triple-negative breast cancer progression by controlling IP3R3 stability. *Mol. Cell Oncol.* **7**, 1813526 (2020).
29. Wang, J. et al. CRIP1 suppresses BBOX1-mediated carnitine metabolism to promote stemness in hepatocellular carcinoma. *EMBO J.* **41**, e110218 (2022).
30. Lindgren, D., Sjolund, J. & Axelson, H. Tracing Renal Cell Carcinomas back to the Nephron. *Trends Cancer* **4**, 472–484 (2018).
31. Lindgren, D. et al. Cell-Type-Specific Gene Programs of the Normal Human Nephron Define Kidney Cancer Subtypes. *Cell Rep.* **20**, 1476–1489 (2017).
32. Smith, J. C. & Sheltzer, J. M. Genome-wide identification and analysis of prognostic features in human cancers. *Cell Rep.* **38**, 110569 (2022).
33. Elias, R. et al. A renal cell carcinoma tumorgraft platform to advance precision medicine. *Cell Rep.* **37**, 110055 (2021).
34. Purdue, M. P. et al. Differences in risk factors for molecular subtypes of clear cell renal cell carcinoma. *Int. J. Cancer* **149**, 1448–1454 (2021).
35. Zvirblyte, J. et al. Single-cell transcriptional profiling of clear cell renal cell carcinoma reveals a tumor-associated endothelial tip cell phenotype. *Commun. Biol.* **7**, 780 (2024).
36. Rebouche, C. J. & Engel, A. G. Tissue distribution of carnitine biosynthetic enzymes in man. *Biochim. Biophys. Acta* **630**, 22–29 (1980).
37. Leung, I. K. et al. Structural and mechanistic studies on gamma-butyrobetaine hydroxylase. *Chem. Biol.* **17**, 1316–1324 (2010).
38. Myllyharju, J. & Kivirikko, K. I. Characterization of the iron- and 2-oxoglutarate-binding sites of human prolyl 4-hydroxylase. *EMBO J.* **16**, 1173–1180 (1997).
39. Hewitson, K. S. et al. Evidence that two enzyme-derived histidine ligands are sufficient for iron binding and catalysis by factor inhibiting HIF (FIH). *J. Biol. Chem.* **283**, 25971–25978 (2008).
40. Vaziri-Gohar, A. et al. Limited nutrient availability in the tumor microenvironment renders pancreatic tumors sensitive to allosteric IDH1 inhibitors. *Nat. Cancer* **3**, 852–865 (2022).
41. Cantor, J. R. et al. Physiologic Medium Rewires Cellular Metabolism and Reveals Uric Acid as an Endogenous Inhibitor of UMP Synthase. *Cell* **169**, 258–272 (2017).
42. Vande Voorde, J. et al. Improving the metabolic fidelity of cancer models with a physiological cell culture medium. *Sci. Adv.* **5**, eaau7314 (2019).
43. Huang, H. et al. L-carnitine is an endogenous HDAC inhibitor selectively inhibiting cancer cell growth in vivo and in vitro. *PLoS One* **7**, e49062 (2012).
44. Lu, Y. et al. Acetylcarnitine Is a Candidate Diagnostic and Prognostic Biomarker of Hepatocellular Carcinoma. *Cancer Res.* **76**, 2912–2920 (2016).
45. Hakimi, A. A. et al. An Integrated Metabolic Atlas of Clear Cell Renal Cell Carcinoma. *Cancer Cell* **29**, 104–116 (2016).
46. Kim, K. et al. Determinants of renal cell carcinoma invasion and metastatic competence. *Nat. Commun.* **12**, 5760 (2021).
47. Osthus, R. C. et al. Deregulation of glucose transporter 1 and glycolytic gene expression by c-Myc. *J. Biol. Chem.* **275**, 21797–21800 (2000).
48. Lu, H. S., Forbes, R. A. & Verma, A. Hypoxia-inducible factor 1 activation by aerobic glycolysis implicates the Warburg effect in carcinogenesis. *J. Biol. Chem.* **277**, 23111–23115 (2002).
49. Cooper, J. M. et al. TBK1 Provides Context-Selective Support of the Activated AKT/mTOR Pathway in Lung Cancer. *Cancer Res.* **77**, 5077–5094 (2017).
50. Kim, J. K. et al. TBK1 Regulates Prostate Cancer Dormancy through mTOR Inhibition. *Neoplasia* **15**, 1064–1074 (2013).
51. Jiang, Q. L., Guan, Y. Y., Zheng, J. M. & Lu, H. D. TBK1 promotes thyroid cancer progress by activating the PI3K/Akt/mTOR signaling pathway. *Immun. Inflamm. Dis.* **11**, https://doi.org/10.1002/iid3.796 (2023).
52. Crew, A. P. et al. Identification and Characterization of Von Hippel-Lindau-Recruiting Proteolysis Targeting Chimeras (PROTACs) of TANK-Binding Kinase 1. *J. Med. Chem.* **61**, 583–598 (2018).
53. Hu, L. et al. TBK1 Is a Synthetic Lethal Target in Cancer with VHL Loss. *Cancer Discov.* **10**, 460–475 (2020).
54. Kishore, N. et al. IKK-i and TBK-1 are enzymatically distinct from the homologous enzyme IKK-2: comparative analysis of recombinant human IKK-i, TBK-1, and IKK-2. *J. Biol. Chem.* **277**, 13840–13847 (2002).
55. Jenkins, R. W. et al. Ex Vivo Profiling of PD-1 Blockade Using Organotypic Tumor Spheroids. *Cancer Discov.* **8**, 196–215 (2018).
56. Larabi, A. et al. Crystal structure and mechanism of activation of TANK-binding kinase 1. *Cell Rep.* **3**, 734–746 (2013).
57. Hu, L. et al. Kinome-wide siRNA screen identifies a DCLK2-TBK1 oncogenic signaling axis in clear cell renal cell carcinoma. *Mol. Cell* **84**, 776–790 e775 (2024).
58. Iliopoulos, O., Kibel, A., Gray, S. & Kaelin, W. G. Tumor Suppression by the Human Von Hippel-Lindau Gene-Product. *Nat. Med.* **1**, 822–826 (1995).
59. Pause, A., Lee, S., Lonergan, K. M. & Klausner, R. D. The von Hippel-Lindau tumor suppressor gene is required for cell cycle exit upon serum withdrawal. *Proc. Natl Acad. Sci. USA* **95**, 993–998 (1998).
60. Hacker, H. & Karin, M. Regulation and function of IKK and IKK-related kinases. *Sci. STKE* **2006**, re13 (2006).
61. Pomerantz, J. L. & Baltimore, D. NF-kappaB activation by a signaling complex containing TRAF2, TANK and TBK1, a novel IKK-related kinase. *EMBO J.* **18**, 6694–6704 (1999).
62. Passarelli, M. C. et al. Leucyl-tRNA synthetase is a tumour suppressor in breast cancer and regulates codon-dependent translation dynamics. *Nat. Cell Biol.* **24**, 307–315 (2022).
63. Gu, Y. F. et al. Modeling Renal Cell Carcinoma in Mice: Bap1 and Pbrm1 Inactivation Drive Tumor Grade. *Cancer Discov.* **7**, 900–917 (2017).
64. Chandrashekar, D. S. et al. UALCAN: An update to the integrated cancer data analysis platform. *Neoplasia* **25**, 18–27 (2022).
65. Liao, C. et al. Integrated Metabolic Profiling and Transcriptional Analysis Reveals Therapeutic Modalities for Targeting Rapidly Proliferating Breast Cancers. *Cancer Res.* **82**, 665–680 (2022).
66. Hew, M. N. et al. Age and gender related differences in renal cell carcinoma in a European cohort. *J. Urol.* **188**, 33–38 (2012).

Acknowledgements

We thank Dr. Haifeng Yang from Thomas Jefferson University, Dr. W. Kimryn Rathmell from Vanderbilt University, and Dr. Peter Ly and Dr. Rashmi Dahiya from UT Southwestern for providing the cell lines. We thank Dr. Pengda Liu and Dr. Zhichuan Zhu from University of North Carolina at Chapel Hill for providing the mTOR plasmid during the revision stage. We acknowledge the assistance of the University of Texas Southwestern Tissue Management Shared Resource, a shared resource at the Simmons Comprehensive Cancer Center, which is supported in part by the National Cancer Institute under award number P30 CA142543. We acknowledge the assistance of the University of Texas Southwestern Medical Center (UTSW) Pre-Clinical Radiation Core Facility, which is supported by CPRIT (RP180770). This research is based in part upon work conducted using the UNC Proteomics Core Facility, which is supported in part by P30 CA016086 Cancer Center Core Support Grant to the UNC Lineberger Comprehensive Cancer Center. This work is partially supported by CPRIT (RR190058, Q.Z.). NIH R01CA256833 and R01CA284591(to Q.Z), and P50CA196516 (to P.K. and J.B.) were used to generate some of resources related to BBOX1 and DCLK2-TBK1 respectively. C.L. is supported by the 2024 Urology Care

Foundation Research Scholar Award Program and Society of Urologic Oncology Specialized Programs of Research Excellence Award.

Author contributions

Conception and design, C.L.; data acquisition, C.L., and L.H.; analysis and interpretation of data, C.L., L.H., L.J., L.D., J.B. and Q.Z.; statistical analysis, L.G., L.X., J.M.S.; administrative, technical, or material support, C.L., L.H., J.Z., T.W., K.K., H.Z., H.Y., Q.L., C.Z., F.Z., J.F., H.L., S.L., S.M., P.K., J.B., R.J.D., and Q.Z.; writing, review, and revision of the manuscript, C.L., J.M.S., J.B., R.J.D., and Q.Z.,; study supervision, C.L. and Q.Z. All authors reviewed and approved the manuscript.

Competing interests

Q.Z. received the consultation fee from Exelixis. Other authors declare no competing interests.

Additional information

Supplementary information The online version contains supplementary material available at https://doi.org/10.1038/s41467-025-56955-y.

Correspondence and requests for materials should be addressed to Chengheng Liao or Qing Zhang.

Peer review information *Nature Communications* thanks Pinglong Xu and the other anonymous reviewer(s) for their contribution to the peer review of this work. A peer review file is available.